Distinct Roles of Kif6 and Kif9 in Mammalian Ciliary Trafficking and Motility

Chuyu Fang[1,2,†], Xinwen Pan[1,3,†], Di Li[4,†], Yawen Chen[1,2], Luan Li[1,2], Qi Gao[1,2], Dong Li[4,*], Xueliang Zhu[1,2,3,5,*] and Xiumin Yan[6,*]

[1] State Key Laboratory of Cell Biology, Shanghai Institute of Biochemistry and Cell Biology, Center for Excellence in Molecular Cell Science, Chinese Academy of Sciences, 320 Yueyang Road, Shanghai 200031, China

[2] University of Chinese Academy of Sciences, Beijing 100049, China

[3] School of Life Science and Technology, ShanghaiTech University, China

[4] National Laboratory of Biomacromolecules, CAS Center for Excellence in Biomacromolecules, Institute of Biophysics, Chinese Academy of Sciences, Beijing, China

[5] School of Life Science, Hangzhou Institute for Advanced Study, University of Chinese Academy of Sciences, Hangzhou 310024, China

[6] Ministry of Education-Shanghai Key Laboratory of Children's Environmental Health, Xinhua Hospital, Shanghai Jiao Tong University School of Medicine, Shanghai 200092, China

[†] Co-first author

* Corresponding author (e-mail: lidong@ibp.ac.cn, xlzhu@sibcb.ac.cn or yanx@shsmu.edu.cn)

Abstract

Ciliary beat and intraflagellar transport (IFT) depend on dynein and kinesin motors. Kinesin-9 family members Kif6 and Kif9 are implicated in ciliary motilities across protists and mammals. How they function and whether they act redundantly, however, remain unclear. Here, we show that they play distinct roles in mammals. Kif6 forms puncta that move bidirectionally without or with IFT-B particles along axonemes, whereas Kif9 is immobilized on ciliary central apparatus. Only Kif6 binds to and glides microtubules, and the activities are self-inhibited. *Kif6* deficiency in mice impairs directional ciliary beat across ependymal tissues and cerebrospinal fluid flow, resulting in severe hydrocephalus and high mortality, whereas *Kif9* deficiency induces mild hydrocephalus without obviously defective ciliary beat and life span. Both *Kif6*$^{-/-}$ and *Kif9*$^{-/-}$ males are infertile but show respectively oligozoospermia with poor sperm motility and defective forward motion of sperms. These results suggest Kif6 as a motile cilia-specific IFT motor and Kif9 as a central apparatus regulator.

Keywords

Basal body; ciliary motility; ependymal cells; hydrocephalus; intraflagellar transport; Kif6; Kif9; kinesin; planar cell polarity

Introduction

Cilia are evolutionarily conserved, microtubule (MT)-based organelles that protrude from the cell surface and are generally categorized into primary and motile cilia (Klena and Pigino, 2022; Reiter and Leroux, 2017). Primary cilia are usually possess 9+0 MT arrangement consisting of nine peripheral doublet MTs (DMTs), whereas most motile cilia/flagella typically possess a 9+2 MT axoneme with a central pair (CP) of MT singlets (C1 and C2) surrounded by nine DMTs (Han et al., 2022; Ishikawa, 2017; Loreng and Smith, 2017). The CP MTs are decorated with proteinaceous projections and the peripheral DMTs are equipped with dynein arms and radial spokes. The signal from CP apparatus transmits through radial spokes to govern the sliding of axonemal dyneins along adjacent MTs, generating cilia/flagella beating (Gui et al., 2021; Hoek et al., 2022; Loreng and Smith, 2017). Except for sperm flagella, motile cilia are mainly present as multicilia with dozens to hundreds of cilia within a single cell in mammals. Multicilia are found in epithelia of various organs such as the brain ventricles, the airway and the oviduct, playing critical roles in cerebrospinal fluid (CSF) circulation, mucus clearance, and ovum transport (Legendre et al., 2021; Marshall and Kintner, 2008; Tissir et al., 2010).

To generate directional fluid flow, proper polarities are needed to establish at both cellular and tissue levels. During the differentiation of multiciliated cells, basal bodies (BBs) initially amplify and dock to the cell membrane, as indicated by the orientiation of their basal feet (BFs), which are conical projections on BB walls that align with the direction of effective strokes (Gibbons, 1961; Mirzadeh et al., 2010; Ohata and Alvarez-Buylla, 2016). As maturation progress, the orientation of BBs within individual cells gradually aligns in a coordinated manner along the direction of fluid flow, establishing rotational polarity (Boutin et al., 2014; Guirao et al., 2010). In ependymal cells, in addition to rotational polarity, BBs exhibit a specific clustering into a patch on one side of the cell surface, establishing translational polarity that distinguishes them from other multiciliated cells such as tracheal epithelial cells (Mirzadeh et al., 2010). These processes ultimately establish the planar

66 polarity of multiciliated tissues. The establishment of planar polarity involves planar cell
67 polarity (PCP) pathway and hydrodynamic force flow, guiding the process over several days
68 (Boutin et al., 2014; Ohata and Alvarez-Buylla, 2016).

69 Kinesins are molecular motors that play essential roles in directional transport of cargos
70 through processive movements along MTs or regulation of MT dynamics in various cellular
71 processes such as mitosis, ciliogenesis and intracellular transport across eukaryotes (Cason
72 and Holzbaur, 2022; Hirokawa et al., 2009; Lu and Gelfand, 2017). They are classified into
73 N-kinesins, M-kinesins, and C-kinesins based on the position of motor domain . Two kinesin
74 families, kinesin-2 and 9, have been found to function in cilia or flagella. The kinesin-2
75 family motors (Kif3a/b/c) are well-known for their involvement in IFT, a specialized
76 bidirectional transportation machinery (Klena and Pigino, 2022; Scholey, 2013). IFT relies on
77 two multi-subunit complexes, IFT-A and IFT-B, which are powered by kinesin-2 or
78 cytoplasmic dynein-2 respectively for anterograde or retrograde trafficking along axonemal
79 MTs in the form of IFT trains (Nakayama and Katoh, 2018). IFT enables the transport of
80 ciliary proteins in and out of cilia, critical for cilia assembly, maintenance, and function
81 (Meleppattu et al., 2022; Nakayama and Katoh, 2018; Pigino, 2021).

82 The kinesin-9 family consists of two members, Kif6 and Kif9, which share a high
83 sequence identity at their motor domains. They belong to the N-kinesin group, typically
84 involved in plus-end-directed transports of cargos (Hirokawa et al., 2009; Lu and Gelfand,
85 2017). Unlike the kinesin-2 family, which plays a critical role in both primary and motile
86 cilia, the kinesin-9 family is predominantly associated with flagellated species (Demonchy et
87 al., 2009; Scholey, 2013), suggesting distinct or redundant roles in regulating flagella
88 motility. In *Chlamydomonas*, only KLP1, the homolog of Kif9, has been studied. It
89 specifically localizes to the CP MTs and is proposed as an active motor to regulate flagellar
90 motility (Bernstein et al., 1994; Han et al., 2022; Yokoyama et al., 2004). Interestingly, in
91 *Trypanosoma*, the kinesin-9 family has been demonstrated distinct functions in flagella
92 motility (Demonchy et al., 2009). Knockdown of *KIF9A*, the *Trypanosoma* homolog of *Kif9*,
93 reduces flagellum beating and cell movement, while knockdown of *KIF9B*, the homolog of

94 *Kif6*, results in cell paralysis and defective assembly of the paraflagellar rod (PFR). Although
95 there is no observed movement of KIF9B within flagella, it is speculated that it is involved in
96 PFR transport or the recognition of axoneme asymmetry for PFR assembly in *Trypanosoma*
97 (Demonchy et al., 2009). In mammals, mutations in *Kif9* have been linked to defective sperm
98 motility and impaired fertility (Meng et al., 2022; Miyata et al., 2020). However, its function
99 in motile cilia remains unexplored. A frameshift mutation of *KIF6* has been found in a patient
100 with intellectual disability and megalocephaly (Konjikusic et al., 2018). Mice carrying a *Kif6*
101 C-terminal truncation mutant (*Kif6*$^{p.G555fs}$) develop severe hydrocephalus possibly due to
102 defective ciliogenesis in the ependyma (Konjikusic et al., 2018). Since the mutant mice still
103 express the motor domain of Kif6, it cannot be ruled out that the observed hydrocephalus
104 phenotype and defective ciliogenesis could be caused by the dominant negative effect of the
105 remaining motor domain. Despite these achievements, a comprehensive understanding of the
106 roles of Kif6 and Kif9 in mammalian ciliary trafficking and cilia motility is still lacking.
107 In this study, we investigate the functions of Kif6 and Kif9 in mice. Our results suggest
108 that Kif6 is a motile cilia-specific motor involved in IFT and essential for the planar polarity
109 of multicilia in the ependyma, whereas Kif9 functions in the central apparatus for regulating
110 cilia/flagella motility.
111

112 **Results**

113 **Mammalian Kif6 and Kif9 are motile cilia-specific kinesins with distinct localizations**

114 Murine full-length Kif6 (NP_796026.2) and Kif9 (NP_001157041.1) are highly
115 conserved proteins composed of 802 and 810 amino acid residues, respectively. Structurally,
116 both proteins have a motor domain located at the N-terminus, followed by two coiled-coil
117 regions and a tail at the C-terminus (Fig. 1a). Their motor domains share a sequence identity
118 of 43%, while their C-termini are less conserved (Fig.1a and Supplementary Fig. 1a, b).
119 Phylogenetic analysis showed that Kif6 and Kif9 co-existed in eukaryotes with motile
120 cilia/flagella, dating back to protists like *Chlamydomonas* and *Tetrahymena* (Fig. 1b and
121 Supplementary Fig. 1a) (Bernstein et al., 1994; Vincensini et al., 2011; Yokoyama et al.,
122 2004). In contrast, they lacked homologues in *Caenorhabditis elegans*, which only contains
123 immotile sensory cilia (Fig. 1b) (Inglis et al., 2007; Vincensini et al., 2011). These data imply
124 that Kif6 and Kif9 are evolved to be both important for motile cilia.

125 We re-analyzed our previous microarray results (Xu et al., 2015) and found that *Kif6* and
126 *Kif9* were highly upregulated during the multiciliation of mouse tracheal epithelial cells
127 (mTECs) (Fig. 1c). Immunoblots confirmed a substantial increase in the protein levels of Kif6
128 and Kif9 during multiciliation of mTECs (Fig. 1d). Furthermore, Kif6 and Kif9 were
129 specifically expressed in tissues and cells abundant in motile cilia or flagella, such as the
130 ependyma, the trachea, the lung, the testis, and primary cultured mouse ependymal cells
131 (mEPCs), but were hardly detected in tissues and cells with only immotile cillia (Fig. 1e, f).
132 Consistently, immunostaining indicated their localizations in motile cilia of mEPCs (Fig. 1g,
133 h) but not in primary cilia of IMCD3 cells (Fig. 1i). To validate their ciliary localization, we
134 infected mEPCs with adenovirus to express Kif6-GFP or Kif9-GFP (Fig. 1g) and clearly
135 observed localizations of the exogenous proteins in motile cilia (Fig. 1j).

136 To visualize their detailed localizations, we performed three dimensional structured
137 illumination microscopy (3D-SIM). Ciliary Kif9 localized in the central lumen of axonemes
138 marked with acetylated tubulin (Ac-tub) and colocalized well with the CP marker Hydin (Fig.
139 1k) (Lechtreck et al., 2008), suggesting a conserved localization in the C2 projection as

140 *Chlamydomonas* KLP1 (Bernstein et al., 1994; Han et al., 2022; Yokoyama et al., 2004). In
141 sharp contrast, Kif6 mainly localized along the axonemes as puncta (Fig. 1k). Similar ciliary
142 localization patterns were observed for GFP-tagged Kif6 and Kif9, using Spef1 as a CP
143 marker (Supplementary Fig. 1c) (Zheng et al., 2019). Therefore, Kif6 and Kif9 appear to play
144 different roles speficifically in motile cilia.

145 **Kif6, but not Kif9, displays IFT-like behaviors along ciliary axonemes**

146 As kinesins with a motor domain at their N-terminus typically function as plus-end-
147 directed motor proteins (Cason and Holzbaur, 2022; Hirokawa et al., 2009), we sought to
148 examine whether GFP-tagged Kif6 and Kif9 expressed in mEPCs (Fig. 2a) could move along
149 DMTs and central MTs, respectively. Immunoblotting demonstrated comparable expression
150 levels of GFP-tagged Kif6 and Ift81, an IFT-B component (Klena and Pigino, 2022), with
151 their endogenous proteins, whereas Kif9-GFP showed relatively higher expression than
152 endogenous Kif9 (Fig. 2b). To achieve superior spatiotemporal resolution, we employed
153 grazing incidence structured illumination microscopy (GI-SIM) (Guo et al., 2018; Qiao et al.,
154 2022). As shown previously (Qiao et al., 2022), Ift81-GFP particles displayed clear
155 bidirectional movements along axonemes (Fig. 2c and Supplementary Fig. 2a; Movie 1).
156 Strikingly, Kif6-GFP puncta also underwent robust and processive bidirectional movements
157 resembling the IFT (Fig. 2d and Supplementary Fig. 2a; Movie 2). Kif9-GFP, however, did
158 not exhibit any processive movement along axonemes (150 cilia from 10 cells) (Fig. 2e and
159 Supplementary Fig. 2a; Movie 3), suggesting that it is immobilized on the central apparatus.

160 Qunatification results revealed that the Kif6-GFP puncta moved at 0.71 ± 0.34 μm/s
161 anterogradely and 0.64 ± 0.34 μm/s retrogradely, similar to those of the Ift81-GFP particles
162 (0.73 ± 0.40 μm/s anterogradely and 0.67 ± 0.36 μm/s retrogradely) (Fig. 2f). Frequencies of
163 movements were also similar between the two (13.3 ± 11.3 and 14.0 ± 10.0 counts/min
164 respectively for anterograde Kif6-GFP puncta and Ift81-GFP particles; 11.0 ± 9.0 and 13.2 ±
165 9.9 counts/min for retrograde Kif6-GFP puncta and Ift81-GFP particles) (Fig. 2g). These
166 results suggest that Kif6 is involved in IFT trafficking.

167 **Ciliary Kif6 puncta traffic with or without IFT-B particles**

168 To understand the relationship between Kif6 and IFT, we immunostained Kif6-GFP-
169 expressing mEPCs to visualize IFT-B component Ift88 or Ift56 (Klena and Pigino, 2022).
170 3D-SIM images showed that some Kif6 puncta were located adjacent to IFT-B particles while
171 the others appeared to be alone (Fig. 3a and Supplementary Fig. 2b).

172 Next, we co-expressed Kif6-GFP and Ift27-Halo, another IFT-B component (Klena and
173 Pigino, 2022), in mEPCs by adenoviral infection and performed dual-color time-lapse GI-
174 SIM imaging. To ensure proper alignment of different fluorescent channels, the microscopic
175 system was calibrated routinely with fluorescent beads prior to imaging (Supplementary Fig.
176 2c). Interestingly, we observed three distinct types of bidirectional movements within cilia:
177 co-moved Kif6-GFP puncta and Ift27-Halo particles ($Ift27^+$ $Kif6^+$ duo-particles), Kif6-GFP
178 puncta alone ($Kif6^+$ particles), and Ift27-Halo particles alone ($Ift27^+$ particles) (Fig. 3b-d and
179 Supplementary Fig. 2d; Movies 4-5). The moving $Kif6^+$ puncta usually left two separate
180 tracks in cilia, similar to the moving $Ift27^+$ particles (Fig. 3b, c and Supplementary Fig. 2d),
181 indicating that their movements are along peripheral doublet MTs instead of central MTs.

182 Quantification analyses on 45 cilia in 4 mEPCs indicated that ratios of these three
183 trafficking types were approximately 1:1.5:1 for both anterograde and retrograde movements
184 (Fig. 3d). These three types of particles exhibited comparable velocities: 0.75 ± 0.32 μm/s
185 ($Ift27^+$ $Kif6^+$), 0.74 ± 0.32 μm/s ($Kif6^+$), and 0.70 ± 0.31 μm/s ($Ift27^+$) anterogradely, or 0.66
186 ± 0.28 μm/s, 0.65 ± 0.34 μm/s, and 0.62 ± 0.28 μm/s retrogradely (Fig. 3e), similar to those
187 measured from mEPCs expressing only one exogenous protein (Fig. 2f).

188 These results suggest that Kif6 traffics bidrectionally in motile cilia as a discrete
189 punctum either with or without an IFT-B particle (Fig. 3f).

190 **Kif6 is a self-inhibited MT-based motor**

191 The trafficking beheviors of Kif6 (Fig. 3) suggested two possibilities: (1) Kif6 might
192 function actively as a processive motor to transport cargos in motile cilia; and (2) Kif6 might
193 only be transported as a passive cargo by IFT trains. To discriminate between these

194 possibilities, we investigated its motor properties. Processive kinesins are self-inhibited by
195 their C-termini and activated either physiologically through cargo binding or artifically by the
196 removal of inhibitory domains (Cason and Holzbaur, 2022; Hirokawa et al., 2009). We thus
197 transiently expressed GFP-Flag-tagged Kif6 or different truncation constructs containing the
198 motor domain in HEK293T cells (Fig. 4a, b) to examine whether Kif6 could bind to MTs *in*
199 *vivo* and whether the binding was regulated in a self-inhibitory manner. We observed that all
200 the truncated constructs (Kif6-CC1, Kif6-CC2, and Kif6-MD) exhibited strong MT
201 localizations, especially on the spindle of mitotic cells (Fig. 4c). Full-length Kif6, however,
202 did not show MT localizations (Fig. 4c). In contrast, neither Kif9 nor its truncation constructs
203 (Kif9-CC1, Kif9-CC2, and Kif9-MD) displayed MT associations (Fig. 4a, c and
204 Supplementary Fig. 3a, b). To clarify whether the robust MT association *in vivo* was a direct
205 effect, we purified the proteins from HEK293T cells (Fig. 3d) and performed MT binding
206 assays *in vitro* (Fig. 4e) (Diao et al., 2022). Consistently, Kif6-CC1, Kif6-CC2, Kif6-MD, and
207 Kif5c-MD, a positive control (Diao et al., 2022), all associated with MTs immobilized on
208 glass coverslips, whereas full-length Kif6 and Kif9-CC1 still did not bind to the MTs (Fig.
209 4f). We next examined whether Kif6-CC1 could actively move along MTs through MT
210 gliding assays (Fig. 4g) (Stanhope and Ross, 2015) and observed that, similar to Kif5c-MD,
211 Kif6-CC1 tethered on coverslips also drove MT gliding (Fig. 4h and Movie 6). Therefore,
212 Kif6 contains an MT-based motor activity that is autoinhibited by its C-terminus and activated
213 presumbly by cargo-binding, supporting its involvement in axonemal MT-based cargo
214 transport in cilia. On the other hand, Kif9's lack of detectable MT-binding or motor activities
215 (Fig. 4) also complies with its immotility on the central apparatus (Fig. 2e), further
216 strengthening its role as an immobilized CP component.

217 **Mice lacking *Kif6* or *Kif9* develop hydrocephalus and exhibit male infertility**

218 To uncover their physiological functions, we generated *Kif6* and *Kif9* knockout mice
219 (Fig. 5a, b) using the CRISPR/Cas9 system (Joung et al., 2017). Immunoblotting confirmed
220 complete depletion of Kif6 or Kif9 in motile cilia-enriched tissues (Fig. 5c). Both *Kif6*$^{-/-}$ and
221 *Kif9*$^{-/-}$ mice were born at the expected Mendelian ratio of genotypes. The majority of *Kif6*$^{-/-}$

222 mice experienced growth failure and often exhibited a dome-shaped skull compared to wild-
223 type littermates after P21, suggestive of severe hydrocephalus (Fig. 5d, arrows). Some of
224 these mice also displayed a forward curvature of the spine and a smaller size compared to
225 their littermates (Fig. 5d, arrowhead). Careful examination of brain dissections or coronal
226 sections revealed that every analyzed *Kif6*$^{-/-}$ mouse (100%; total n = 60) displayed lateral
227 ventricle expansion when compared to the wild-type controls (Fig. 5f, h). This ventricle
228 enlargement was evident even in mice that displayed a normal skull appearance and longer
229 lifespan (Fig. 5f, bottom). In sharp contrast to *Kif6*$^{-/-}$ mice, *Kif9*$^{-/-}$ mice appeared normal
230 similar to their wild-type littermates based on macroscopic examination (Fig. 5e). However,
231 coronal brain sections revealed enlarged ventricles in over half of *Kif9*$^{-/-}$ mice (Fig. 5g, h),
232 indicative of hydrocephalus. Survival curve analysis revealed that approximately 77% of *Kif6*$^{-}$
233 $^{/-}$ mice died before reaching P90, while *Kif9*$^{-/-}$ mice exhibited a normal lifespan similar to their
234 wild-type littermates during a 12-month observation period (Fig. 5i).

235 While female *Kif9*$^{-/-}$ and *Kif6*$^{-/-}$ mice were fertile, *Kif9*$^{-/-}$ and *Kif6*$^{-/-}$ males were sterile,
236 even when those with normal appearance were used for mating (n = 3 for each genotype).
237 Subsequently, we isolated sperms from the cauda epididymis of wild-type, *Kif9*$^{-/-}$ and *Kif6*$^{-/-}$
238 mice at reproductive age (~ 2 months) for motility analysis. *Kif9*$^{-/-}$ male mice showed a slight
239 decrease in sperm count compared to wild-type controls (Supplementary Fig. 4a, b). Although
240 *Kif9*$^{-/-}$ sperms had normal morphologies, they displayed impaired progressive motilities (Fig.
241 5j, k and Movie 7), consistent with previous report (Miyata et al., 2020). *Kif6*$^{-/-}$ mice,
242 however, showed a significant reduction in sperm count (Supplementary Fig. 4c, d).
243 Interestingly, while *Kif6*$^{-/-}$ sperms appeared to be normal in morphologies (Fig. 5k), the
244 majority of them completely lacked motilities (67%, total n = 46) as compared to wild-type
245 sperms (3%, n = 131) (Movie 8). In contrast to these, we did not observed noticeable defects,
246 such as polydactyly or polycystic kidney, in organs where primary cilia are critical (Nachury
247 and Mick, 2019), suggesting intact primary cilia functions. These observations emphasize the
248 critical yet distinct roles of Kif6 and Kif9 in motile cilia and sperm flagella.

249 ***Kif6* but not *Kif9* deficiency disrupts the planar polarity of ependymal motile cilia**

250 The planar beating of ependymal multicilia in mice older than P21 generates
251 unidirectional CSF flow in brain ventricles (Guirao et al., 2010; Ohata and Alvarez-Buylla,
252 2016). As abnormalities in mouse ependymal cilia cause hydrocephalus (Ji et al., 2022; Liu et
253 al., 2021; Ohata et al., 2014), we dissected the brain of >P21 mice and stained multicilia in
254 living ependymal tissues with SiR-tubulin, a fluorescent probe for MTs (Lukinavicius et al.,
255 2014), followed by live imaging using high-speed spinning disk confocal microscopy (Fig.
256 6a). We did not observe gross differences in multiciliogenesis, the back-and forth beat pattern
257 of multicilia, and their beat frequency between *Kif6*$^{+/+}$ and *Kif6*$^{-/-}$ or *Kif9*$^{+/+}$ and *Kif9*$^{-/-}$
258 littermates (Fig. 6b-e and Movies 9, 10). Nevertheless, while multicilia beat directionally
259 across different cells in the wild-type or *Kif9*$^{-/-}$ ependymal tissues, their beat directions
260 differed among individual cells in *Kif6*$^{-/-}$ ependymal tissues regardless of the hydrocephalus
261 severity of the mice (Fig. 6f, g and Movies 9, 10), indicating a disruption in the planar
262 polarity of *Kif6*$^{-/-}$ multicilia (Ohata and Alvarez-Buylla, 2016).
263 Next, we investigated whether the loss of planar beating impaired directional fluid flow
264 across *Kif6*$^{-/-}$ ependymal tissues by adding latex fluorescent microbeads to the culture medium
265 and tracking their movements by live imaging (Fig. 6h). We observed that the beads
266 underneath wide-type ependymal tissues flew in one direction with a velocity of 63.6 ± 27.1
267 μm/s (Fig. 6i, j and Movie 11). In contrast, the beads underneath *Kif6*$^{-/-}$ ependymal tissues
268 mainly oscillated or whirled regionally, with a velocity of 46.3 ± 15.4 μm/s (Fig. 6i, j and
269 Movie 12). Therefore, we attribute the hydrocephalus of *Kif6*$^{-/-}$ mice (Fig. 6) to impaired CSF
270 flow.
271 **Kif6 is crucial for the rotational polarity of BBs in ependymal tissues**
272 For insights into why *Kif6*$^{-/-}$ multicilia lost the planar polarity of beat directions (Fig. 6),
273 we performed transmission electron microscopy with ependymal tissues to examine cilia-
274 related ultrastructure (Fig. 7a). Cross-sections indicated that *Kif6*$^{-/-}$ ependymal cilia still
275 contained 9+2 axonemes, with outer and inner dynein arms on DMTs (Fig. 7b). Nevertheless,
276 the image resolutions were still insufficient for a definite conclusion whether the entire

277 axonemal ultrastructure was the same as the wild-type one (Fig. 7b) (Meng et al., 2023).
278 Interestingly, we observed that, while BFs were oriented towards a similar direction in the
279 wild-type ependymal cells, a state termed the rotational polarity of BBs (Ohata and Alvarez-
280 Buylla, 2016), BFs in *Kif6*$^{-/-}$ ependymal cells were misoriented regardless of the severity of
281 hydrocephalus (Fig. 7c). To quantify the extent of the rotational polarity, we considered each
282 arrow marking the BF orientation as a unit vector and measured the mean vector length for
283 each electron micrograph (Bustamante-Marin et al., 2019). The proper rotational polarity of
284 BBs in the wild-type ependymal tissues was confirmed by a mean vector length of 0.97 ±
285 0.07. In sharp contrast, the value was 0.35 ± 0.17 and 0.31 ± 0.18 for ependymal tissues from
286 mice respectively with mild and severe hydrocephalus (Fig. 7d).
287 As transmission electron microscopy is not ideal for assessing BB polarities in entire
288 cells, letting alone planar polarities, we immunostained whole-mounts of ependyma from wild
289 type, *Kif6*$^{-/-}$, or *Kif9*$^{-/-}$ mice using Cep164, a transition fiber component (Siller et al., 2017), to
290 mark BBs, and γ-tubulin or Centriolin to label BFs (Nguyen et al., 2020; Ohata et al., 2014).
291 3D-SIM revealed a uniform rotational polarity of BBs in individual cells and a planar polarity
292 among neighboring cells in both wild type and *Kif9*$^{-/-}$ wholemounts (Fig. 7e-g and
293 Supplementary Fig. 5a-c). Both the rotational and the planar polarities of BBs, however, were
294 markedly impaired in *Kif6*$^{-/-}$ ependymas (Fig. 7e-g and Supplementary Fig. 5a-c). We also
295 scored BB numbers and observed that the deficiency of either *Kif6* or *Kif9* did not interfere
296 with the BB biogenesis (Supplementary Fig. 5d), consistent with the normal ciliogenesis (Fig.
297 6) but different from the reported defective ciliogenesis in *Kif6*$^{p.G555fs}$ mice (Konjikusic et al.,
298 2018).
299 In addition to the rotational polarity, BBs in ependymal cells form patches that tend to be
300 positioned towards one side of the cell border, a state termed the translational polarity
301 (Mirzadeh et al., 2010; Ohata and Alvarez-Buylla, 2016). We quantified the extent of BB
302 patch displacement relative to the cell center (Mirzadeh et al., 2010) but did not observe a
303 significant change between the wild-type mice and their *Kif6*$^{-/-}$ littermates (Supplementary
304 Fig. 5e-g). The area of BB patches was also unaffected in *Kif6*$^{-/-}$ mice with mild

305 hydrocephalus but slightly increased in mice with severe hydrocephalus (Supplementary Fig.
306 5e, f, h), possibly due to the pathological effects of the hydrocephalus.
307 Taken together, we conclude that Kif6 is critical for the rotational polarity of BBs but
308 dispensable for the transitional polarity. The defective rotational polarization in *Kif6*$^{-/-}$
309 ependymas abolishes the planar polarity of ciliary beat, leading to abnormal CSF flow and
310 hydrocephalus.
311

312 **Discussion**

313 In this study, we elucidated the distinct ciliary localizations and functions of Kif6 and
314 Kif9, two kinesin-9 family members in mammalian motile cilia (Fig. 1b and 7h). Kif9 is
315 mainly found in the CP lumen in motile cilia, while Kif6 as puncta localizes and moves
316 bidirectionally with or without IFT-B particles along the DMTs (Figs. 1-3 and Supplementary
317 Figs. 1-2). Interestingly, neither Kif6 nor Kif9 are necessary for ciliogenesis (Fig. 6).
318 However, *Kif6* knockout disrupts cilia motility coordination (Fig. 6 and Movie 10) and
319 impaired sperm motility (Fig. 5l and Movie 8), and leads to hydrocephalus (Fig. 4d, f, h) and
320 male infertility in mice. *Kif9* knockout results in male infertility by affecting sperm forward
321 motility (Fig. 5k and Movie 7) and a mild hydrocephalus (Fig. 5g, h) possibly due to a defect
322 in fine-tuning the cilia beating.

323 IFT is responsible for bidirectional transportation of ciliary proteins. The kinesin-2
324 family motors, including Kif3a/3b/3c and Kif17, facilitate the anterograde IFT, which is
325 essential for ciliogenesis of both primary and motile cilia across species (Klena and Pigino,
326 2022; Scholey, 2013; Zhao et al., 2012). Compared to IFT in primary cilia, IFT in motile cilia
327 transports a wide variety of large protein complexes, including dynein arms, radial spokes,
328 and proteins critical for cilia beating. Futhermore, the axonemal MTs of motile cilia are
329 frequently decorated with an array of associated proteins or protein complexes and exhibit
330 rapid beating (Gui et al., 2021; Han et al., 2022; Ma et al., 2019). These differences suggest
331 that IFT in motile cilia may possess unique features or require additional molecular motors.
332 Remarkably, using high-speed and super-resolution GI-SIM, we performed the first dual-
333 colour imaging of particles trafficking within mammalian motile cilia. We discovered that
334 Kif6, but not Kif9, undergoes processive movement in ependymal cilia (Figs. 2-3 and
335 Supplementary Fig. 2; Movies 2-5). The bidirectional movement of Kif6 along the ciliary
336 axoneme, either with or without IFT-B particles (Fig. 3 and Supplementary Fig. 2d), together
337 with its ability to bind and glide along MTs, implies that Kif6 may transport cargos either
338 independently or in association with the IFT-B-containing IFT train (Fig. 7h). This finding

339 suggests the possibility of separate protein transport mechanisms, warranting further
340 investigation. It is important to note that the presence of endogenous proteins can not
341 currently be ruled out in IFT-B free Kif6 puncta. The presence of Kif6 in single-cell
342 organisms such as *Chlamydomonas* and *Trypanosoma*, which contain motile cilia/flagella
343 (Bernstein et al., 1994; Demonchy et al., 2009), suggest its conserved role in IFT.
344 In *Trypanosoma*, the lack of *KIF9B*, a *Kif6* homolog, disrupts the assembly of the PFR, a
345 structure asymmetrically assembled at DMTs 4-7 along the flagellar axoneme, required for
346 flagellar motility (Demonchy et al., 2009; Zhang et al., 2021). While the PFR is exclusive to
347 euglenoids and kinetoplastids (Cachon et al., 1988; Langousis and Hill, 2014), the "9+2"
348 mammalian motile cilia also display asymmetrical structures enabling the back-and-forth
349 ciliary beat (Ishikawa, 2017; Loreng and Smith, 2017). The ciliary beat direction is
350 perpendicular to the CP plane from DMT 1 to the gap between DMT 5 and 6 (axonemal
351 orientations), and the direction of BFs aligns with the effective stroke of cilia (BB polarities)
352 (Butler and Wallingford, 2017; Clare et al., 2014; Lindemann and Lesich, 2021; Ohata and
353 Alvarez-Buylla, 2016). Our recent study reveal that axonemal orientations and BB polarities
354 are initially decoupled and gradually become aligned during the development of multiciliated
355 ependyma (Pan et al., 2023). This process requires both the PCP pathway and external flow
356 force. *Kif6* deficiency does not affect translational polarity of BBs, but it does disrupt the
357 rotational polarity of BBs and planar polarity of cilia in ependyma (Figs. 6-7 and
358 Supplementary Fig. 5; Movie 10). Since PCP pathway is key for translational polarity
359 (Mirzadeh et al., 2010; Ohata and Alvarez-Buylla, 2016), Kif6 likely does not function
360 upstream of the PCP pathway. Instead, it may transport specific cargos containing factors
361 important for hydrodynamic force responses or the axoneme-BF coupling (Fig. 7h) (Guirao et
362 al., 2010; Pan et al., 2023; Tissir et al., 2010). This idea is supported by the misalignment of
363 BBs in *Kif6*$^{-/-}$ mice, similar to obervations in cultured mEPCs lacking external flow force
364 (Guirao et al., 2010). Furthermore, this speculation is also reinforced by the observation that
365 *Kif6*$^{-/-}$ mice do not exhibit noticeable airway defects. The rotational polarity of BBs in tracheal
366 epithelial cells can align correctly in the absence of flow forces *in vitro* (Herawati et al.,

367 2016). In the future, identifying molecules or factors associated with Kif6 could provide more
368 insights into its function and the regulatory mechanism.
369 The immobilization of Kif9 within ependymal cilia is consistent with the observation in
370 *Xenopus* epidermal multiciliated cells (Konjikusic et al., 2023), reinforcing the notion that
371 Kif9 is not involved in ciliary transport. In flagellated species *Trypanosoma* and
372 *Chlamydomonas*, knockdown *Kif9* homolog, lead to a reduction flagella movement (Bernstein
373 et al., 1994; Demonchy et al., 2009; Yokoyama et al., 2004). High-resolution structures of
374 *Chlamydomonas* by cryo-electron microscopy (Cryo-EM) shows that the Kif9 homolog,
375 KLP1, exhibits an 8-nm sliding on the C2 MT and is proposed to function as an active motor
376 to power the movement of the central apparatus for regulating flagella beating (Han et al.,
377 2022). Considering the conserved CP localization from protists to mammals and defective
378 sperm motility and hydrocephalus upon its depletion in mice (Fig. 5g, h, k and Movie 7), it
379 could be hypothesized that mammalian Kif9 as a central apparatus regulator for cilia/flagella
380 beating, through mediating conformation changes of central apparatus during beating (Fig.
381 7h). Future studies employing advanced technologies such as cryo-electron tomography
382 technology (Cryo-ET) studies will be needed to validate this hypothesis.
383
384

385 **Methods**

386 **Plasmids**

387 The cDNAs encoding full-length *Kif6* (GenBank: NM_177052.3), *Kif9* (GenBank:
388 NM_001163569.1), *Ift81* (GenBank: NM_001358917.1), and *Ift27* (GenBank:
389 NM_025931.3) were amplified using PCR with cDNAs extracted from cultured mEPCs (Day
390 10) as the template. To generate adenoviral expression constructs, the cDNAs fragments were
391 PCR-amplified and subsequently cloned into the entry vector pYr-1.1-GFP (YRBio, China) or
392 pYr-1.1-Halo to express GFP-tagged or Halo-tagged proteins, respectively. The LR
393 recombination reactions between the entry constructs and the destination vector
394 pAd/BLOCK-iT-DEST (YRBio, China) were carried out using LR Clonase II enzyme mix
395 (Thermo Fisher, 11791020), as described previously (Zhao et al., 2021).

396 The rat Kif5c-MD-GFP (1-430 aa) construct was kindly provided by Prof. Bao (Institute
397 of Biochemistry and Cell Biology, CAS). To express GFP-fusion proteins, the cDNAs of Kif6
398 (1-802 aa), Kif6-MD (1-353 aa), Kif6-CC1 (1-385 aa), Kif6-CC2 (1-494 aa), Kif9 (1-810 aa),
399 Kif9-MD (1-348aa), Kif9-CC1 (1-442 aa) and Kif9-CC2 (1-694 aa) were amplified and
400 subcloned into pEGFP-N1. To express GFP-Flag-fusion proteins, the cDNAs of Kif6-GFP,
401 Kif6-MD-GFP, Kif6-CC1-GFP, Kif6-CC2-GFP, Kif9-GFP, Kif9-MD-GFP, Kif9-CC1-GFP,
402 Kif9-CC2-GFP and Kif5c-MD-GFP were amplified and constructed into pCDAN3.1-CFlag.
403 To generate polyclonal antibodies of Kif9, the cDNA fragments encoding the indicated amino
404 acids (348-810 aa) were amplified by PCR and subcloned into pET-28a or pGEX-4T-1, to
405 express His-tagged or GST-tagged Kif9, respectively.

406 All constructs were validated by sequencing. The primers used for PCR amplification are
407 listed in Supplementary Table 1.

408 **Mice**

409 All animal experiments were performed following guidelines approved by the Institutional
410 Animal Care and Use Committee of Institute of Biochemistry and Cell Biology. The mice
411 used in this study had a genetic background of C57BL/6J. *Kif6*$^{+/-}$ and *Kif9*$^{+/-}$ mice were
412 obtained from GemPharmatech, China. Ages of mice used in this study were indicated in the
413 figures or the legends. gRNA sequences used for targeting *Kif6* or *Kif9* and primers used for

414 genotyping are listed in Supplementary Table 1.

415 **Cell culture and transfection**

416 HEK293T and HEK293A cells were grown in Dulbecco's modified Eagle's medium
417 (DMEM) (Thermo Fisher, 12430-054) supplemented with 10% fetal bovine serum (FBS)
418 (Ausbian, VS500T), 0.3 mg/ml glutamine (Sigma, G8540), 100 U/ml penicillin (Solarbio,
419 P8420) and 100 U/ml streptomycin (Solarbio, S8290). NIH3T3 cells were cultured in DMEM
420 medium with 10% normal goat serum (NGS), 0.3 mg/ml glutamine, 100 U/ml penicillin, and
421 100 U/ml streptomycin. hTERT-RPE1 and IMCD3 cells were cultured in DMEM/F12
422 medium (GE Healthcare) supplemented with 10% FBS, 0.3 mg/ml glutamine, 100 U/ml
423 penicillin, and 100 U/ml streptomycin. Additionally, RPE1 culture medium was supplemented
424 with 10 μg/ml hygromycin B (Thermo Fisher). All cell lines were passaged at a 1:4 ratio once
425 they reached 80%-90% confluency. HEK293A cells were used for packaging adenovirus
426 expressing GFP-tagged proteins following the guidelines (YRBio, China). All the cells were
427 routinely tested for mycoplasma contamination.

428 Primary culture of mouse ependymal cells (mEPCs) was prepared and cultured as
429 previously described (Delgehyr et al., 2015; Zhao et al., 2021). Newborn C57BL/6J mice
430 were anesthetized on ice, and the cerebellum, olfactory bulbs, meninges, and hippocampus
431 were carefully removed using sharp tweezers (Dumont, 1214Y84) in cold dissection solution
432 (5 mM Hepes, 161 mM NaCl, 5 mM KCl, 1 mM $MgSO_4$, 3.7 mM $CaCl_2$, and 5.5 mM
433 Glucose, pH 7.4) under a stereo microscope. The remaining telencephala were then digested
434 in a dissection solution containing 10 U/ml papain (Worthington-Biochem, LS003126),
435 0.2 mg/ml L-cysteine, 1.5 mM NaOH, 1 mM $CaCl_2$, 0.5 mM EDTA, and 0.15% DNase I
436 (Sigma-Aldrich, D5025) for 30 min at 37°C. After gentle pipetting and centrifugation at 1,500
437 rpm for 5 min at room temperature (r.t.), the cells were resuspended in DMEM medium
438 supplemented with 10% FBS and 1% penicillin/streptomycin and seeded into flasks (Sigma-
439 Aldrich, L2020) pre-coated with 10 μg/ml Human Plasma Fibronectin (Sigma-Aldrich,
440 FC010). Neurons were mechanically shaken off and removed by patting the flask
441 approximately 2 days after inoculation. When reaching ~90% confluence, cells were digested
442 with trypsin and re-plated into fibronectin-coated 29-mm glass-bottomed dishes (Cellvis,
443 D29-14-1.5-N) for immunofluorescence staining. Once cells were cultured to ~90%

444 confluency, FBS was removed from the medium to induce differentiation.

445 For the primary culture of mTECs, we followed the method described (Zhao et al.,
446 2021). mTECs were used to investigate the expression profile of *Kif6* and *Kif9* during the
447 differentiation of mTECs, because of their high induced differentiation efficiency.

448 For transfection of plasmids, cells were transfected at ~70% confluency with
449 Lipofectamine 2,000 (Thermo Fisher).

450 **Preparation and culture of whole-mounts of lateral ventricle walls**

451 Whole-mounts of the lateral ventricles were prepared as described (Ohata et al., 2014)
452 with minor modifications. Mice were euthanized with CO_2, and the lateral ventricles were
453 carefully dissected at a thickness of 500-1000 μm using Vannas Scissors (66VT, 54140B) in
454 pre-warmed (37°C) dissection solution (25 mM Hepes,117.2 mM NaCl, 5.3 mM KCl,
455 0.81 mM $MgSO_4$, 1.8 mM $CaCl_2$, 26.1 mM $NaHCO_3$, 1 mM $NaH_2PO_4 \cdot 2H_2O$, and 5.6 mM
456 Glucose, pH 7.4). The samples were subsequently cultured in DMEM supplemented with 0.3
457 mg/ml glutamine, 100 U/ml penicillin, and 100 U/ml streptomycin.

458 **Viral production and transfection**

459 Adenovirus particles were utilized to infect mEPCs or IMCD3 cells and produced in
460 HEK293A cells as previously described (Zhao et al., 2021). In brief, the adenovirus
461 expression constructs were linearized using *P*acI restriction enzyme (NEB) and transfected
462 into HEK293A cells cultured in 6-well plates using Lipofectamine 2,000 to produce the initial
463 adenovirus. When approximately 80% of the cells exhibited a cytopathic effect (CPE), the
464 culture medium was collected and infected HEK293A cells in a 10-cm dish. Once about 80%
465 of the cells showed a CPE, the culture medium was collected to infect fresh HEK293A cells
466 for viral amplification. When ~80% of the cells exhibited a CPE, both cells and the culture
467 medium were collected. To ensure complete release of the viral particles, three freeze-thaw
468 cycles (-80°C and 37°C) were performed, followed by centrifugation at 1,500 rpm for 5 min
469 to remove cell debris. The harvested adenoviral particles were used at a dilution of 1:1000 or
470 1:200.

471 **Immunofluorescence staining and imaging**

472 IMCD3 cells were fixed with 4% paraformaldehyde (PFA) in PBS, whereas mEPCs
473 grown on 29 mm glass-bottom dishes and freshly dissected whole-mounts were pre-

474 permeabilized with 0.5% Triton X-100 in PBS for 30 sec before fixation to remove soluble
475 proteins. After fixation, the cells were extracted with 0.5% Triton X-100 in PBS for 15 min
476 and blocked in 4% BSA in TBST at r.t. for 1 h. Next, the cells were incubated with primary
477 antibodies overnight at 4°C. After three washes with the blocking solution for 5 min each, the
478 cells were incubated with secondary antibodies at r.t. for 1h, and mounted in Dako (Dako,
479 S3023) or ProLong™ (Thermo Fisher, 2273640). All the antibodies used are listed in
480 Supplementary Table 2.

481 Fluorescent images were captured using a Leica TCS SP8 WLL system with a HC PL
482 APO CS2 63 × /1.40 OIL objective or an Olympus Xplore SpinSR10 microscope with
483 UPLAPO OHR 60 ×/1.50 Objective Lens, and images were processed with maximum
484 intensity projections. 3D-SIM super-resolution images were taken with a DeltaVision OMX
485 SR system (GE Healthcare) and the z-axis scanning step was 0.125 μm. The original images
486 were processed for OMX SI Reconstruction, OMX Image Registration, and maximum
487 intensity projection with SoftWoRx software.

488 To perform GI-SIM imaging for mEPCs, the cells were seeded onto fibronectin-coated
489 12-mm coverslips and were infected with adenovirus one day prior to serum starvation. To
490 fluorescently label their multicilia, mEPCs were incubated with 100 nM SiR-tubulin
491 (Spirochrome, SC002) for 30 min or 200 nM Janelia Fluor® 549 HaloTag ligand (Promega,
492 GA1110) for 20 min. After labeling, mEPCs were gently laid flat against the bottom coverslip
493 and GI-SIM imaging was performed as described (Guo et al., 2018; Qiao et al., 2022). For
494 dual-color imaging, instrument calibration was conducted routinely with fluorescent beads.
495 The images and movies were processed using Fiji and Huygens softwares. The velocities and
496 frequencies of GFP or Halo-tagged particles were manually analyzed by kymographs with Fiji
497 software as previously described (Lechtreck, 2013). For analyzing particle frequencies, we
498 only used the first 200 frames of a recording to avoid potential bleaching of the signal over
499 the time course of image capture.

500 To record ciliary beating, the whole mounts of lateral ventricles were dissected and cut at
501 a thickness of 500-1000 μm as previously described (Ohata et al., 2014; Zhao et al., 2021). To
502 label the cilia, 100 nM SiR-tubulin was added to the culture medium and incubated for 1 h.
503 High-speed live imaging was conducted at 37°C using an Olympus Xplore SpinSR 10

504 microscope equipped with UPLAPO OHR 60 × /1.50 Objective Lens, Hamamatsu ORCA-
505 Fusion camera, 4,000 rpm CSU Disk Speed, and OBIS Laser. Ciliary beat was captured at
506 100 frames per second (fps) by a time-lapse collection of single optical sections with 80%
507 laser power (640 nm) to achieve an exposure time of 5 ms. Kymographs were generated for
508 the first 500 ms using Fiji.

509 The ependymal flow assay was performed as described (Liu et al., 2021; Mirzadeh et al.,
510 2010) with minor modifications. Briefly, the freshly dissected ependyma was sliced using a
511 vibratome (Leica VT1000S) to obtain slices with a thickness of 250 μm. Before imaging,
512 multicilia were labeled with 100 nM SiR-tubulin for 1 h and small fluorescent latex beads
513 with a diameter of 250 nm at 1:500 dilution (Invitrogen, F8809) were added to the culture
514 medium. Time-lapse microscopy was performed at 37 °C using using an Olympus Xplore
515 SpinSR10 microscope equipped with UPLAPO OHR 60 × /1.50 Objective Lens. The laser
516 power for the beads channel (561 nm) was adjusted based on the fluorescent intensity, and
517 exposure time was set to 100 ms. The laser power for the SiR-tubulin channel (640 nm) was
518 set to 80% to achieve an exposure time of 5 ms.

519 During recording, fluorescent beads suspended in the culture medium containing the
520 living ependymal tissues were imaged at a fixed z-plane to record their motility.
521 Subsequently, multicilia in the same areas were visualized by adjusting the focal plane, and
522 live imaging of a single optical section was conducted to record ciliary motility. All frames of
523 beads in the same area were projected together from Movies 12-13 and superimposed with
524 trajectories of traceable, rapidly-moving bead aggregates in the first 500 ms to show flow
525 directions and tracks. The velocity of beads was meausured using Fiji.

526 To record sperm motility, sperm were released from cauda epididymidis into buffer
527 (Njabsw, M1130), and followed by live imaging with a spinning disk confocal microscope at
528 a fixed z-plane and at 25-ms intervals. Sperms from two pairs of P88 wild-type and *Kif6*$^{-/-}$
529 litermates and two pairs of P80 of wild-type and *Kif9*$^{-/-}$ litermates littermates were examined.
530 For analyzing sperm number, we randomly select the first frame (full micrograph with 2304 ×
531 2304 pixels) of a recording and only count the sperm with head from each genotype. For
532 analyzing sperm head displacement, we randomly select a recoding last for 1 second to trace
533 the clear sperm movement and then measure the head displacement.

534 **Protein purification**

535 Protein purification was performed as described (Liu et al., 2021). Cells were lysed with
536 cold lysis buffer (20 mM Tris-HCl, pH 7.5, 100 mM KCl, 0.1% NP-40, 1 mM EDTA, 10 mM
537 $Na_4O_7P_2$, 10% Glycerol, and protease inhibitors (Sigma, 539134)). The lysates were collected
538 after centrifugation for 20 min at 13,000 rpm at 4°C to remove debris. The precleared lysates
539 were incubated with 20 μl of anti-FLAG beads (Sigma, A2220) for 2 hr at 4°C under rotary
540 agitation. The beads were washed three times with the lysis buffer and three times with wash
541 buffer (20 mM TrisHCl, pH 7.5, 150 mM KCl, 0.5% NP-40, 1 mM EDTA, 10 mM $Na_4P_2O_7$,
542 10% Glycerol). The proteins on the FLAG beads were eluted with 30 μl of 1 mg/ml FLAG
543 peptide and were ready for *in vitro* MT binding and gliding assays.

544 **Immunoblotting**

545 Immunoblotting experiments were performed as described (Zhao et al., 2021). To
546 prepare tissue lysates, freshly dissected tissues from mice were placed in ice-cold RIPA buffer
547 (50 mM Tris-HCl, 150 mM NaCl, 1% NP-40, 0.5% Sodium Deoxycholate, 0.1% SDS, and 1
548 mM EDTA, pH7.5) supplemented with protein inhibitors cocktail. The tissues were
549 homogenized using the homogenizer Precellys 24 system (Bertin, France). The lysates were
550 cleared by centrifugation at 13,200 rpm at 4°C for 15 min, and mixed with an equal volume of
551 2 × SDS-PAGE loading buffer (100 mM Tris-HCl, 4% SDS, 20% glycerol, 2% 2-
552 mercaptoethanol, 0.1% bromophenol blue, pH 6.8). For cultured cells, cells were washed with
553 pre-warmed PBS and lysed in 2 × SDS-PAGE loading buffer. The lysates were boiled at
554 100°C for 10 min and then subjected to immunoblotting.

555 ***In-vitro* MT binding and gliding assays**

556 To assemble the imaging chamber, two pieces of double-slided tape were adhered to a
557 clean microscope slide and a silanized 18 mm × 18 mm glass coverslip was placed and
558 pressed onto the double-sided tape, creating a chamer between the coverslip and the
559 microscope slide as previously described (Stanhope and Ross, 2015). For MT binding assay, a
560 solution containing 10 μg/μl of Streptavidin was diluted in 50 ul of reaction buffer and
561 pipetted into the imaging chamber, followed by immobilization for 20 min and blocking with
562 1% (w/v in ddH_2O) Pluronic F127 for 10 min. For MT gliding assay, the purified kinesin
563 proteins were nonspecific adsorbed onto the surface of a coverslip and immobilized.

564 To perform MT binding assay, rhodamine-labeled MTs were polymerized using a
565 mixture containing 5% rhodamine-labeled tubulin (Cytoskeleton, TL590M), 5% biotin-
566 labeled tubulin (Cytoskeleton, T333P), and 90% unlabeled tubulin (Cytoskeleton, T240) in
567 BRB80 buffer (80 mM PIPES, 1 mM EGTA ,1 mM $MgCl_2$, pH 6.8) supplemented with 1 mM
568 GTP. The mixture was then incubated at 37°C for 30 min. Next, 10 μM taxol was added, and
569 the incubation continued at 37°C for an additional 30 min to stabilize the MTs. The sample
570 was subsequently centrifuged at 13, 200 rpm for 25 min to remove free tubulin. The
571 polymerized MTs were diluted in BRB80 buffer and introduced into an imaging chamber,
572 allowing them to adsorb to the coverslips via streptavidin. Subsequently, the motor proteins,
573 along with 1 mM ATP in BRB80 buffer, were added to the polymerized MTs and imaged
574 using a total internal reflection fluorescent (TIRF) microscope (ZEISS Cell Observer SD).
575 To perform MT gliding assays, rhodamine-labeled GMPCPP-stabilized MT seeds were kindly
576 donated from Prof. Bao (Institute of Biochemistry and Cell Biology, CAS) and utilized as
577 previously described (Diao et al., 2022; Stanhope and Ross, 2015). 3 μM Kif6-CC1 or 2 μM
578 Kif5c-MD in BRB80 supplemented with 1 mM ATP and incubated for 5 min to pre-coated the
579 glass surfaces. Subsequently, rhodamine-labeled GMPCPP-stabilized MT seeds plus 1 mM
580 ATP in BRB80 buffer were introduced to examine the gliding ability of the MTs along the
581 coverslip surface. The dynamic gliding of MTs was imaged using a TIRF microscopy at 0.72-
582 s interval for per frame.

583 **Transmission electron microscopy**

584 The tissues were fixed in 2.5% glutaraldehyde/PBS at 4°C overnight, washed with PBS,
585 and treated with 1% OsO_4 for 1.5 h at r.t.. The tissues were dehydrated with a graded series of
586 ethanol and further dehydrated with acetone. Subsequently, the samples were embedded in
587 Epon 812 resin at 60°C for 48 h. Thin sections of 70 nm thickness were obtained using an
588 ultramicrotome (Leica EM PACT2) and stained with 2% uranyl acetate for 15 min, followed
589 by 1% lead citrate for 5 min. The images were captured using a FEI Tecnai G2 Spirit Twin
590 transmission electron microscope and analyzed using Fiji software.

591 **Coronal brain section**

592 Coronal brain slices with a thickness of 250 μm were achieved using a vibratome
593 sectioning technique, as previously described (Chen et al., 2020). Mice were deeply

594 anesthetized with 360 mg/kg body weight of avertin administered via intraperitoneal
595 injections. Transcardial perfusion was performed using PBS followed by 4% PFA in PBS,
596 utilizing an injection pump (Smiths medical, WZS-50F6, 250 ml/h). Whole brains were
597 dissected from the mice and cut using a vibratome to obtain coronal slices with a thickness of
598 250 μm. These slices were placed into 35-mm glass-bottom dishes (Cellvis, D35-20-1.5-N)
599 and were imaged with an Olympus SZX16 Stereo Microscope.

600 **Reproductive performance test**

601 Mating test was perform as previously described (Miyata et al., 2020). 2-3 month-old
602 *Kif6*$^{-/-}$ and *Kif9*$^{-/-}$ male mice with normal appearance were individually caged with two age-
603 appropriate heterozygous female mice for four months and two *Kif6*$^{-/-}$ and *Kif9*$^{-/-}$ female mice
604 were separately caged with one heterozygous male mice, and then were checked regularly
605 every several days. The number of pups was counted during the period. Three independent
606 experiments were carried out.

607 **Phylogenomic analysis and multiple alignment**

608 The phylogenetic tree and taxonomic groups were constructed based on literatures and
609 Taxonomy Browser of National Center for Biotechnology Information (NCBI) (Cetkovic et
610 al., 2018; Mukherjee and Brocchieri, 2013). The protein database of NCBI were searched to
611 identify genes with orthologous proteins of Kif6 and Kif9 across a wide range of species
612 (such as mammals, birds, amphibians, fishes, jawless vertebrates, cephalochordates,
613 urochordates, echinoderms, nematodes, mollusks, flatworms, cnidarians, placozoans and
614 protozoans) using the full-length murine protein sequences of Kif6 and Kif9 as queries.

615 The selected sequences were aligned using COBALT searches with default settings.
616 Genebank accession numbers of Kif6 and Kif9 orthologues were provided in Supplemenatry
617 Figure 1a. Only alignment columns without gaps were colored, with highly conserved
618 positions shown in red and less conserved positions shown in blue.

619 **Analysis of BB rotational polarity**

620 BB rotational polarity was analyzed as previously described (Guirao et al., 2010;
621 Mirzadeh et al., 2010; Ryu et al., 2021). In TEM images, the BB rotational polarity was
622 determined by drawing a unit vector from the center of a BB to the vertex of its BF. The mean

vector length within a given field in each full-size electron micrograph (2,048 pixels × 2,048 pixels) was calculated using Microsoft Excel software (Microsoft). In 3D-SIM images, the BB rotational polarity was determined by drawing a unit vector from the geographic center of Cep164 ring (BB distal end marker) to the center of either Centriolin or γ–tubulin signals (BF marker). The mean vector length within a cell was calculated using Excel software (Microsoft) to demostrate the extent of the rotational polarity.

Quantification and statistical analysis

BB numbers were assessed without knowledge of the genotypes and were measured from 3D-SIM images using Cep164-positive ring as a BB marker. The BB center and cell border center were determined using the default setting of the "ROI Manager" function in Fiji.

All experiments, unless otherwise stated, were independently repeated at least twice for both microscopic or biochemical results. Statistical results are presented as mean ± SD. Unpaired two-tailed student's *t*-test was performed using GraphPad Prism 9.0 software, and differences were considered significant at $P < 0.05$. Data analyses were performed in a blinded manner, with the researchers performing the quantification being unaware of the genotype.

Acknowledgements.

The authors thank Profs. Lan Bao and Dr. Lei Diao (Shanghai Institute of Biochemistry and Cell Biology, CAS) for the reagents and technical assistance, Profs. Xin Liang (Tsinghua University) and Profs. Wei Feng (Institute of Biophysics, CAS) for technical help and valuable discussions, and the staff members of the Integrated Laser Microscopy System at the National Facility for Protein Science in Shanghai (NFPS) (Shanghai Advanced Research Institute, CAS) and core facilities of the Center for Excellence in Molecular Cell Science (CEMCS) for instrumental and technical supports. This work was supported by National Natural Science Foundation of China (31991192, 32230027 and 32270725).

Declaration of interests

The authors declare no competing financial interests.

Author contributions

X.Y., X.Z., and Dong L. conceived and supervised the project; C.F., X.P. and Di L.

performed the research; Dong L. provided GI-SIM; Y.C., L.L. and Q.G. assisted with experiments; X.Y., X.Z., C.F. and X.P. collectively analyzed data and wrote the manuscript, with input from all authors.

657 **Figure legends**

658 **Figure 1. Molecular characterizations and subcellular localizations of mammalian *Kif6***
659 **and *Kif9*. (a)** Schematics of full-length murine Kif6 and Kif9. The motor and coiled-coil
660 domains were identified using Conserved Domain Search Service of NCBI and SMART
661 (Simple Modular Architecture Research Tool) (http://smart.embl.de). **(b)** Conservation of *Kif6*
662 and *Kif9* across species with motile cilia and/or flagella throughout the evolution process. The
663 phylogenetic tree and taxonomic groups were referrenced from literature (Cetkovic et al.,
664 2018; Mukherjee and Brocchieri, 2013). **(c)** mRNA expression profiles of *Kif6* and *Kif9*
665 during multiciliation. The gene expression profiles were obtained from our previous cDNA
666 microarray analysis of mTECs cultured at an air-liquid interface (ALI) for the indicated days
667 (Xu et al., 2015). Expression patterns of genes crucial for cilia formation (*Ift88* and *Ift122*)
668 and BB amplification (*Cep152*), were listed for comparison (Klena and Pigino, 2022; Zhao et
669 al., 2013). **(d)** Expression patterns of Kif6 and Kif9 during multiciliation of mTECs.
670 Multicilia formation is indicated by increased levels of Ift81, Bbs3 and acetylated tubulin
671 (Ac-tub) (Klena and Pigino, 2022). Gapdh served as loading control. **(e, f)** Abundance of Kif6
672 and Kif9 in mouse tissues (**e**) and cultured cells (**f**) containing motile cilia. Tissues from a 2-
673 month-old male mouse were dissected and lysed. mEPCs were harvested on day 8 post serum
674 starvation. RPE1, NIH3T3 and IMCD3 cells were serum-starved for 48 h to induce
675 ciliogenesis. Gapdh or β-actin served as loading control. **(g)** Experimental scheme for **h, j, k**
676 and Supplementary Fig. 1c. Precursors of mEPCs were isolated from P0 mouse brain and
677 serum-starved on day 0 to induce to differentiate into multiciliated cells. To express GFP-
678 tagged proteins, the cells were infected with adenovirus on day-1. The cells were fixed on day
679 8 for immunofluorescence (IF) staining and imaged by confocal microscopy (**h**, **j**) or 3D-SIM
680 (**k**). **(h)** Localizations of endogenous Kif6 and Kif9 in motile cilia. Ac-tub labeled ciliary
681 axonemes. Arrowheads indicate typical cilia. **(i)** Kif6 and Kif9 did not localize in primary
682 cilia. IMCD3 cells were serum-starved to induce primary ciliogenesis and fixed at day 2 post
683 serum starvation for IF, followed by confocal microscopy. The nucleus was visualized by

684 DAPI, a DNA-specific dye. Cilia pointed by arrowheads were zoomed in 2× to show details.
685 **(j)** Exogenous Kif6-GFP and Kif9-GFP localized at the axonemes of multicilia. **(k)** Typical
686 3D-SIM images of endogenous Kif9 and Kif6. Ac-tub and Hydin served as axoneme and CP
687 markers, respectively. Cilia pointed were magnified by 200% for details. Corresponding line
688 scans at the indicated region of the magnified insets showed colocalizations of Kif9 with
689 Hydin and of Kif6 with Ac-tub. Illustrations are provided to aid comprehensions.

690 **Figure 2. Kif6 moves along axonemes in IFT-like pattern and Kif9 is immobilized on the**
691 **central apparatus.** Quantification results are presented as mean ± SD and subjected to
692 unpaired two-tailed student's *t*-test. **(a)** Experimental scheme for ciliary trafficking recorded
693 by GI-SIM. mEPCs were infected with adenovirus at day-1 and imaged during days 5-8. **(b)**
694 Expression levels of GFP-tagged proteins in day 7 mEPCs. Immunoblotting was performed
695 using GFP, Kif6, Kif9 and Ift81 antibodies, respectively. A star indicates a non-specific band
696 closed to Ift81-GFP. **(c-e)** Ciliary movement of Ift81-GFP (**c**), Kif6-GFP (**d**) and Kif9-GFP
697 (**e**). Both Ift81-GFP (**c**) and Kif6-GFP (**d**) were able to move along the axonemal outer DMTs
698 while the motility of Kif9-GFP (**e**) was not detectable. Images were recorded at 25 frames per
699 sec (fps). The trafficking trajectories of GFP-tagged puncta through time projections of the
700 first 200 frames from Movies 1-3 were showed. Typical cilia framed by dashed red lines in
701 projected images, were magnified by 300% to show details. Dash green lines were used to
702 outline the cilia. The clear and traceable particles were marked respectively by arrowheads for
703 anterograde and by arrows for retrograde to show the progressive movements. The
704 corresponding kymographs were presented. (**f, g**) Quantification results of velocities and
705 frequencies from the indicated numbers of particles (**f**) and cilia (**g**). Antero: Anterograde
706 transport; Retro: Retrograde transport; s: second.

707 **Figure 3. Kif6-GFP puncta move with or without IFT-B particles along the DMTs. (a)**
708 Typical 3D-SIM images of Kif6-GFP and IFT proteins (Ift56 and Ift88). Cilia cropped from
709 Supplementary Fig. 2b were magnified by 400% to show details. Ac-tub marked ciliary
710 axoneme. Line scans at the indicated regions (I-IV) exihibited the Kif6-GFP with or without

711 IFT proteins, which were respectively pointed by arrowheads or arrows. **(b-f)** Ciliary
712 trafficking of fluorescent particles. mEPCs were infected with adenovirus expressing of Kif6-
713 GFP and Ift27-Halo and were performed dual-color time-lapse live imaging at 14 fps. Three
714 distinct bidirectional moving particles within cilia were observed: labeled with both Ift27-
715 Halo and Kif6-GFP ($Ift27^{+}Kif6^{+}$ duo-particles), only with Kif6-GFP ($Kif6^{+}$ particles) and only
716 with Ift27-Halo ($Ift27^{+}$ particles). Ciliary trafficking trajectories of GFP/Halo-tagged puncta
717 were projected by the first 200 frames from Movies 4-5. Typical trajectories pointed were
718 magnified by 300% to roughly outline the cilia in projected images. The clear and traceable
719 particles were indicated to display anterograde (arrowheads) and retrograde (arrows)
720 transports of $Ift27^{+}Kif6^{+}$ duo-particles (**b**), $Kif6^{+}$ particles (**c**) and $Ift27^{+}$ particles (**c**) from
721 representative time sequences. Dashed green lines were used to outline the cilia.
722 Corresponding kymographs were presented. The ratios (**d**) and velocities (**e**) of these three
723 distinct trafficking particles were quantified from 45 cilia in 4 mEPCs. The number (n) of
724 corresponding particles was presented. Refer to Supplementary Fig. 2d for additional example
725 of $Kif6^{+}$ or $Ift27^{+}$ bidirectional movements. Illustration is provided to aid comprehensions (**f**).

726 **Figure 4. Kif6 but not Kif9 binds and glides MTs. (a)** Diagrams of Kif6 and its deletion
727 constructs showing their MT-binding ability. Kif5c-MD (1-430 aa) served as a positive
728 control (Diao et al., 2022; Rogers et al., 2001). N/D, not determine. **(b)** Schematic of HEK293T
729 cells culture and following analyses. HEK293T cells were transfected for 48 h and harvested
730 for immunostaining (**c**) or protein purification (**d**). **(c)** Motor domain of Kif6 was required for
731 spindle MTs binding. MTs were visualized by an anti-α-tubulin antibody. Chromosomes and
732 nuclei were stained with DAPI. **(d)** Commassie blue-staining of purified proteins. Kif5c-MD
733 was purified to serve as a positive control. **(e)** Schematic of *in-vitro* MT binding assays using
734 total internal reflection fluorescence (TIRF) microscopy. Fluorescently labeled GMPCPP-
735 stabilized microtubules immobilized on a Pluronic F127-treated glass coverslip via
736 strepavidin linkages were imaged after the addition of GFP-tagged kinesin (final
737 concentration: 0.5 μM) and ATP (1 mM). **(f)** The motor domain of Kif6, but not Kif9, bounds

738 to MTs *in vitro*. **(g)** Schematic of *in-vitro* MT gliding assays using TIRF microscopy. Kif6-
739 CC1 or Kif5c-MD were pre-immobilized on a coverslip and fluorescently labeled MTs were
740 added for the assay. **(h)** Kif6-CC1 drove MT gliding. Arrowheads pointed to the moving
741 MTs. Representative images were cropped from Movie 6.

742 **Figure 5. Knockout of *Kif6* or *Kif9* leads to hydrocephalus and male infertility. (a)**
743 Schematic for generating *Kif6* (top) and *Kif9* (bottom) knockout mice using CRISPR/Cas9
744 technique. The targeting of sgRNA (scissors) and genotyping PCR primers were indicated for
745 each knockout model. **(b)** Representative genotyping PCR results. Genomic DNAs were
746 extracted from P21 mice tails and amplified by PCR using the indicated primers in (**a**). **(c)**
747 Complete depletion of Kif6 and Kif9 proteins in the indicated tissues. Tissue lysates were
748 prepared from 2-month-old mice of the indicated genotypes. Gapdh served as a loading
749 control. **(d, e)** Morphologies of *Kif6* and *Kif9* deficient mice. *Kif6*$^{-/-}$ mice exhibited a dome-
750 shaped skull (arrow) and kyphosis (arrowhead) with skinny bodies (**d**). In contrast, *Kif9*$^{-/-}$
751 mice showed a normal appearance (**e**). **(f, g)** Representative images of coronal brain sections
752 of *Kif6*$^{-/-}$ (**f**) or *Kif9*$^{-/-}$ (**g**) and their corresponding wide-type littermates. M: month. **(h)**
753 Quantification of mice with enlarged brain ventricles (n = 60 for *Kif6*$^{-/-}$; n = 11 for *Kif9*$^{-/-}$
754 mice). **(i)** Survival curves of mice in indicated genotypes during a 12-month observation
755 period. The number (n) of mice used for each genotype were indicated. **(j)** Sperm morphology
756 from wide-type and *Kif9*$^{-/-}$ littermates. **(k)** *Kif9* deficiency exhibited sperm forward motility
757 defects. Quantification results of sperm head displacement (μm) within 1 second from two
758 mice each genotype (10 movies per mouse) were pooled together (mean ± SD plus sample
759 dots) and subjected to unpaired two-tailed student's *t*-test. Two pairs of P80 *Kif9*$^{-/-}$ mice and
760 wild-type liitermates were used. The indicated sperm numbers (n) were presented. **(l)** Sperm
761 morphology from wide-type and *Kif6*$^{-/-}$ littermates. Two pairs of P88 *Kif6*$^{-/-}$ mice and wild-
762 type litermates were used.

763 **Figure 6. Knockout of *Kif6* impairs planar polarity of cilia across the ependyma.**
764 Quantification results are pooled together (mean ± SD plus sample dots) and subjected to

765 unpaired two-tailed student's *t*-test. Mi: mild hydrocephalus mice with normal appearance but
766 larged ventricles; Se: severe hydrocephalus mice with the observable dome-shaped skull like
767 Figure 1d. **(a)** Schematic of experimental design. Whole-mounts of ventricle walls were
768 freshly dissected and subjected to electron microscopy (EM) or live cell imaging. SiR-tubulin,
769 a fluorescent dye for MTs, was used to label cilia. Ciliary motility was live-cell imaged at a
770 single optical section with 10-ms intervals. An illustration of the beat pattern of an ependymal
771 cilium, depicted as a side view, is provided for better comprehension. **(b-e)** The directional
772 ciliary beat in ependymal cells and ciliary beat frequencies of the indicated genotypes. No
773 gross differences were observed in the back-and forth beat pattern of multicilia (**b**, **d**) and
774 their beat frequencies (**c**, **e**) between *Kif6*$^{+/+}$ and *Kif6*$^{-/-}$ or *Kif9*$^{+/+}$ and *Kif9*$^{-/-}$ littermates. Two
775 consecutive cycles of cilia beat patterns were showed and color coded arrows were used to
776 indicate the patterns. The first cycle of cilia beating was pseudo-colored and merged (**b**, **d**).
777 Quantification of ciliary beating frequencies (**c**, **e**). Results were from 5 pairs of littermates
778 with 60 cells per mouse for (**c**) or 3 pairs of littermates with 50 cells per mouse for (**e**). **(f)**
779 Unidirectional multicilia beat across ependyma was disrupted by the loss of *Kif6*. The first
780 three consecutive frames cropped from Movies 9-10, were pseudo-colored and overlaid to
781 show ciliary motilities. Beating directions of multicilia are indicated by arrows. **(g)** Planar
782 polarity of cilia beating was not altered in *Kif9*-deficient ependyma. **(h)** Schematic
783 illustrations forthe beads assay. Fluorescent beads, suspended in culture medium, were
784 imaged in areas covered with ependymal tissues. The imaging was performed at a fixed z-
785 plane, with an exposure time of 100 ms per frame to record the motilities of the beads. **(i)**
786 Representative projections of bead movements from Movies 11-12. Trajectories of traceable,
787 rapidly-moving beads in the first 500 ms were superimposed to show flow directions. **(j)**
788 Quantification of bead velocities. Results from two pairs of P36 and one pair of P48
789 littermates, with 60 traceable beads for each.

790 **Figure 7. *Kif6* deficiency impairs rotational polarity of BBs in ependymal tissues.**
791 Quantification results are pooled together (mean ± SD plus sample dots) and subjected to
792 unpaired two-tailed student's *t*-test. Se: Severe hydrocephalus mice with obvious dome-
793 shaped skull. Mi: mild hydrocephalus mice with normal morphological appearance but
794 enlarged ventricles. **(a)** Schematic diagram of a motile cilium and an uniformed rotational

795 polarity of BBs. A side view of a motile cilium and transverse views of the axoneme and the
796 BB were presented. BB polarity is denoted by their conical BFs that extend laterally to the
797 MT triplets. **(b)** Representative transmission electron microscopy images showed transverse
798 views of the axoneme of ependymal cilia from wild-type and *Kif6*$^{-/-}$ mice (n = 2 biological
799 replicates). **(c, d)** Representative transmission electron microscopy images (**c**) and
800 quantification analysis on the extent of rotational polarity (**d**). BF orientations are indicated
801 by arrows. The mean vector length (**d**) was calculated from BBs with clear BFs in at least ten
802 full-size electron micrographs and over 130 BFs were scored for each genotype. **(e-g)** The
803 loss of *Kif6*, but not *Kif9*, impaired rotational polarity. Ependymal tissues from the indicated
804 mice were immunostained for Cep164 to visualize BBs and γ-tubulin to visualize BFs.
805 Framed regions (**e**) were magnified to show the rotational polarity of BBs in individual cells
806 **(g)**. The BF orientations are indicated by arrows. Note the misorangized rotational polarity in
807 both cellular and tissue-level in *Kif6*$^{-/-}$ ependyma. Mean vector lengths (**f**) were scored from
808 20 cells each mouse. Mice used were two 6-month-old (6M) and one 7-month-old (7M) mice
809 for *Kif9*$^{-/-}$ and three of their wild-type littermates; two P34, one P43 mice with severe
810 hydrocephalus and one P62 mouse with mild hydrocephalus for *Kif6*$^{-/-}$ and their
811 corresponding wild-type littermates. **(h)** A summary model. Kif6 acts as a motile cilia-
812 specific IFT motor, either on its own or in association with the IFT-B-containing IFT train.
813 On the other hand, Kif9 localizes on the central apparatus to modulate detailed ciliary beat
814 forms, possibly by inducing conformational changes in the central apparatus as a C2
815 projection (Han et al., 2022). BB, basal body; BF, basal foot; TZ, transition zone.

816 **Legends for Supplementary Figures**

817 **Supplementary Figure 1. Conservations and ciliary localizations of Kif6 and Kif9**
818 **(related to Fig. 1). (a)** Similarities of Kif6 (left) and Kif9 (right) orthologues, obtained using
819 constraint-based multiple alignment tool (COBALT) in NCBI. Highly conserved positions are
820 shown in red and less conserved positions shown in blue. Protein sequences of Kif6
821 orthologues used were: mouse (NP_796026.2), human (NP_659464.3), chicken
822 (XP_003640993.5), frog (NP_001106482.1), zebrafish (NP_001070899.1), lancelet
823 (XP_035685117.1), ascidian (XP_002124970.1), sea urchin (XP_030854411.1), mussel

824 (CAG2221785.1), flatworm (PAA61917.1), sea anemone (XP_032228212.2), *Trichoplax*
825 (RDD42533.1), *Tetrahymena* (XP_001024804.2), *Trypanosoma* (XP_846346.1) and green
826 algae (XP_042928646.1). Protein sequences of Kif9 orthologues used were: mouse
827 (NP_001157041.1), human (NP_001400904.1), chicken (XP_040522129.1), frog
828 (XP_012821147.1), zebrafish (XP_001922460.1), lancelet (XP_035663761.1), ascidian
829 (XP_018668035.1), sea urchin (XP_030830023.1), mussel (CAG2242108.1), flatworm
830 (PAA61899.1), sea anemone (XP_001636554.1), *Trichoplax* (RDD45058.1), *Tetrahymena*
831 (XP_001022313.1), *Trypanosoma* (RHW71316.1) and green algae (P46870.1). **(b)** Sequence
832 alignment of Kif6 and Kif9 motor domains, generated by the COBALT sequence alignment
833 program using default parameters. GenBank accession numbers of proteins were as follows:
834 NP_796026.2 (Kif6) and NP_001157041.1 (Kif9). The motor domains were identified using
835 SMART. **(c)** Localizations of exogenous Kif6 and Kif9 in motile cilia. Cultured mEPCs were
836 treated as indicated in Figure 1g to express Kif6-GFP or Kif9-GFP and imaged by 3D-SIM.
837 Spef1 and acetylated tubulin (Ac-tub) served as markers for the CP and the axoneme,
838 respectively. Typical cilia (arrowheads) were magnified by 200% to highlight details. Line
839 scans were generated at the indicated positions by white lines in merged images.

840 **Supplementary Figure 2. Kif6 moves along the axoneme with or without IFT-B particles**
841 **(related to Fig. 2 and 3). (a)** Kif6-GFP, but not Kif9-GFP, resembling Ift81-GFP, moved
842 along the axonemal DMTs. The trafficking trajectories of GFP-tagged puncta were visualized
843 through projections of the first 200 frames. Typical cilia framed by dashed red lines in
844 projected images were magnified by 300% to showed details. Dashed green lines were used to
845 outline the cilia. The clear and traceable GFP-tagged particles were marked and
846 corresponding kymographs were presented. **(b)** Co-immunostainning Kif6-GFP with IFT
847 proteins (Ift56 and Ift88) imaged by 3D-SIM. The framed cilia were magnified and presented
848 in Figure 3a. Ac-tub marked ciliary axoneme. (**c**) Calibration of the microscope. Instrument
849 calibration was conducted routinely with fluorescent beads before dual-color GI-SIM imaging
850 experiments. A line scan was performed along the white line to determine the alignment. **(d)**
851 Ciliary trafficking trajectories of GFP/Halo-tagged puncta were projected by the first 200
852 frames. Typical cilia pointed were magnified by 300% to show details. Dashed green lines

853 were used to outline the cilia. Kif6^{+} particles or Ift27^{+} particles are indicated by colored
854 arrowheads or arrows to respectively show anterograde or retrograde transports from image
855 time sequences. Corresponding kymographs were presented.

856 **Supplementary Figure 3. Kif9 does not exhibit MT associations in HEK293T cells**
857 **(related to Fig. 4). (a)** Diagrams of Kif9 and its deletion constructs showing their MT-
858 binding ability. **(b)** Kif9 and its deletion constructs displayed no spindle MTs binding. MTs
859 were visualized by an anti-α-tubulin antibody. Chromosomes and nuclei were stained with
860 DAPI, a DNA-specific dye.

861 **Supplementary Figure 4. *Kif6*-deficient and *Kif9*-deficient males show decreased sperm**
862 **number (related to Fig. 5).** Sperm were released from cauda epididymis, followed by a
863 spinning disk confocal microscope at a fixed z-plane. Representative images (**a, c**) were from
864 cauda epididymis of littermates. Quantification results (**b, d**) from two mice each genotype (5
865 full-size micrographs per mouse) were pooled together (mean ± SD plus sample dots) and
866 subjected to unpaired two-tailed student's *t*-test.

867 **Supplementary Figure 5. *Kif6* deficiency disrupts rotational polarity but not the**
868 **translational polarity of BBs in ependyma (related to Fig. 7).** Se: Severe hydrocephalus
869 mice with obvious dome-shaped skull. Mi: mild hydrocephalus mice with normal
870 morphological appearance but enlarged ventricles. **(a-c)** BBs in *Kif6*$^{-/-}$ but not in *Kif9*$^{-/-}$
871 ependymal cells displayed impaired rotational polarity. Ependymal tissues from the indicated
872 littermates were co-immunostained for Cep164 to visualize BBs and Centriolin to visualize
873 BFs. Framed regions in (**a**) were maginified to show BFs orientations (arrows). Framed
874 regions in (**c**) were presented in (**a**). Arrows in (**c**) indicate rotational polarities of the wild-
875 type and *Kif9*$^{-/-}$ BB patches, which broadly point to one direction in the microscopic field.
876 Quantification of the rotational polarity **(b)**. Results from three mice per genotype were
877 presented as mean ± SD plus sample dots and subjected to unpaired two-tailed student's *t*-test.
878 Mice used were: two 6-month-old (6M) and one 7-month-old (7M) mice for *Kif9*$^{-/-}$ and three
879 of their wild-type littermates; three P35 mice with severe hydrocephalus for *Kif6*$^{-/-}$ and three
880 of their wild-type littermates. 20 ependymal cells were scored for each mouse. **(d)** BB number
881 in ependymal cells was not altered by *Kif6* or *Kif9*-deficiency. 50 cells were measured per

882 mouse. **(e-h)** *Kif6* deficiency did not impair the transitional polarity of BBs. Ependymal
883 tissues from two P62 and one P68 *Kif6*$^{-/-}$ mice of mild hydrocephalus, three severe
884 hydrocephalus (P34, P38 and P43) and three wild-type mice (P62, P38, and P43) were
885 immunostained for ZO1 and Cep164 to visualize cell borders and BBs, respectively (**e**). BB
886 patch displacement relative to the cellular geographic center (**g**) and relative BB patch area
887 (**h**) were quantified as illustrated in (**f**). 50 ependymal cells were scored for each mouse.

888

889 **Legends for supplementary movies**

890 **Movie 1. Bidirectional motility of ciliary Ift81-GFP puncta (related to Fig. 2c).** mEPCs
891 were infected with adenovirus at day-1 and imaged during day 5-8 by GI-SIM. Images were
892 recorded at 25 frames per sec (fps) and the playback speed is 20 fps. Typical cilia framed
893 were magnified by 300% to show details of Ift81-GFP puncta. The clear particles were
894 marked by arrowheads or arrows to show anterograde or retrograde transports, respectively.

895 **Movie 2. Bidirectional motility of ciliary Kif6-GFP puncta (related to Fig. 2d).** mEPCs
896 were treated, imaged, and presented as described in Movie 1. Typical cilia framed were
897 magnified by 300% to show detailed bidirectional transports of Kif6-GFP puncta. The
898 traceable particles were indicated by arrowheads or arrows to show anterograde or retrograde
899 transports, respectively.

900 **Movie 3. Kif9-GFP does not exhibit progressive movement along the cilia (related to Fig.**
901 **2e).** mEPCs were treated, imaged, and presented as described in Movie 1. Typical cilia framed
902 were magnified by 300% to show details.

903 **Movie 4. Ciliary Kif6-GFP puncta move together with IFT-B particles (related to Fig.**
904 **3b).** mEPCs were infected with adenovirus expressing Kif6-GFP and Ift27-Halo, and dual-
905 color time-lapse live imaging was taken by GI-SIM. Images were recorded at 14 fps and the
906 playback speed is 20 fps. Typical cilia pointed were magnified by 300% to display clear
907 anterograde (arrowheads) and retrograde (arrows) transports of Ift27^{+}Kif6^{+} duo-particles.

908 mEPCs were infected with adenovirus at day-1 and imaged during day 5-8 by GI-SIM.
909 Images were recorded at 25 fps and the playback speed is 20 fps.

910 **Movie 5. Ciliary Kif6-GFP puncta move without IFT-B particles (related to Fig. 3c).**
911 mEPCs were treated, imaged, and presented as described in Movie 4. Typical cilia pointed
912 were magnified by 300% to display traceable anterograde (arrowheads) and retrograde
913 (arrows) transports of Kif6^{+} particles or Ift27^{+} particles (related to Fig. 3c).

914 **Movie 6. The MT gliding of Kif6-CC1 (related to Fig. 4h).** Kif5c-MD served as a positive
915 control. 2 μM Kif6-CC1 (left) or 2 μM Kif5c-MD (right) respectively in BRB80
916 supplemented with 1 mM ATP. Yellow arrowheads indicate the gliding MTs. The assay was
917 acquired at 0.72s/frame. The playback speed is 10 fps.

918 **Movie 7. A representative sperm motility from *Kif9*$^{+/+}$ and *Kif9*$^{-/-}$ male mice.** Sperms were
919 released from cauda epididymis, followed by live imaging with a spinning disk confocal
920 microscope at a fixed z-plane and at 25-ms intervals. The playback speed is 20 fps. One pair
921 of P80 wild-type (left) mice and *Kif9*$^{-/-}$ (right) litermates were presented.

922 **Movie 8. A representative sperm motility from *Kif6*$^{+/+}$ and *Kif6*$^{-/-}$ male mice.** Sperm were
923 released, imaged, and presented as described in Movie 7. One pair of P88 wild-type (left)
924 mice and *Kif6*$^{-/-}$ (right) litermates were presented.

925 **Movie 9. Representative ciliary beat patterns in *Kif6*$^{+/+}$ ependyma (related to Fig. 6f).**
926 The P31 *Kif6*$^{+/+}$ ependyma was freshly dissected and labeled with SiR-tubulin, followed by
927 live imaging with a spinning disk confocal microscope at a fixed z-plane and at 10-ms
928 intervals. The playback speed is 5 fps. Images of the first three frames are presented in Figure
929 6f.

930 **Movie 10. Representative ciliary beat patterns in *Kif6*$^{-/-}$ ependyma (related to Fig. 6f).**
931 The P31 *Kif6*$^{-/-}$ ependyma was treated, imaged, and presented as described in Movie 9. The
932 mouse used was a littermate of the one in Movie 9, and exhibited severe hydrocephalus.
933 Images of the first three frames are presented in Figure 6f.

934 **Movie 11. Representative liquid flows were driven by ciliary beat in *Kif6*$^{+/+}$ ependyma**
935 **(related to Fig. 6i).** Fresh ependyma from a P36 wild-type mouse were incubated with SiR-
936 tubulin to label cilia and fluorescent latex beads as flow indicators. Beads motilities were
937 imaged with a spinning disk confocal microscope at 100-ms intervals and at a fixed z-plane.
938 The playback speed is 5 fps. Trajectories of 8 traceable, rapidly-moving aggregated beads in
939 the first 500 ms were shown. The projections of bead movements are presented in Figure 6i.

940 **Movie 12. Representative liquid flows were driven by ciliary beat in *Kif6*$^{-/-}$ ependyma**
941 **(related to Fig. 6i).** Fresh ependymal tissues from a P36 *Kif6*$^{-/-}$ mouse with severe
942 hydrocephalus were treated, imaged, and presented as described in Movie 13. Trajectories of
943 13 traceable, rapidly-moving aggregated beads in the first 500 ms were shown. The
944 projections of bead movements are presented in Figure 6i.

945 **Legends for Supplementary Tables**

946 **Supplementary Table 1 Sequences of primers and gRNAs.**
947 **Supplementary Table 2 List of antibodies.**

948
949
950
951
952
953
954
955
956
957

References

1. Bernstein, M., Beech, P.L., Katz, S.G., and Rosenbaum, J., L. (1994). A New Kinesin-like Protein (Kip1) Localized to a Single Microtubule of the Chlamydomonas Flagellum. J Cell Biol *125*, 1313-1326.
2. Boutin, C., Labedan, P., Dimidschstein, J., Richard, F., Cremer, H., Andre, P., Yang, Y., Montcouquiol, M., Goffinet, A.M., and Tissir, F. (2014). A dual role for planar cell polarity genes in ciliated cells. Proc Natl Acad Sci U S A *111*, E3129-3138.
3. Bustamante-Marin, X.M., Yin, W.N., Sears, P.R., Werner, M.E., Brotslaw, E.J., Mitchell, B.J., Jania, C.M., Zeman, K.L., Rogers, T.D., Herring, L.E.*, et al.* (2019). Lack of GAS2L2 Causes PCD by Impairing Cilia Orientation and Mucociliary Clearance. Am J Hum Genet *104*, 229-245.
4. Butler, M.T., and Wallingford, J.B. (2017). Planar cell polarity in development and disease. Nat Rev Mol Cell Biol *18*, 375-388.
5. Cachon, J., Cachon, M., Cosson, M.-P., and Cosson, J. (1988). The paraflagellar rod: a structure in search of a function. Biology of the Cell *63*, 169-181.
6. Cason, S.E., and Holzbaur, E.L.F. (2022). Selective motor activation in organelle transport along axons. Nat Rev Mol Cell Biol *23*, 699-714.
7. Cetkovic, H., Harcet, M., Roller, M., and Bosnar, M.H. (2018). A survey of metastasis suppressors in Metazoa. Lab Invest *98*, 554-570.
8. Chen, Y., Zheng, J., Li, X., Zhu, L., Shao, Z., Yan, X., and Zhu, X. (2020). Wdr47 Controls Neuronal Polarization through the Camsap Family Microtubule Minus-End-Binding Proteins. Cell Rep *31*, 107526.
9. Clare, D.K., Magescas, J., Piolot, T., Dumoux, M., Vesque, C., Pichard, E., Dang, T., Duvauchelle, B., Poirier, F., and Delacour, D. (2014). Basal foot MTOC organizes pillar MTs required for coordination of beating cilia. Nat Commun *5*.
10. Delgehyr, N., Meunier, A., Faucourt, M., Bosch Grau, M., Strehl, L., Janke, C., and Spassky, N. (2015). Ependymal cell differentiation, from monociliated to multiciliated cells. Methods Cell Biol *127*, 19-35.
11. Demonchy, R., Blisnick, T., Deprez, C., Toutirais, G., Loussert, C., Marande, W., Grellier, P., Bastin, P., and Kohl, L. (2009). Kinesin 9 family members perform separate functions in the trypanosome flagellum. J Cell Biol *187*, 615-622.
12. Diao, L., Liu, M.Y., Song, Y.L., Zhang, X., Liang, X., and Bao, L. (2022). alpha1A and alpha1C form microtubules to display distinct properties mainly mediated by their C-terminal tails. J Mol Cell Biol *13*, 864-875.
13. Gibbons, I.R. (1961). The relationship between the fine structure and direction of beat in gill cilia of a lamellibranch mollusc. J Biophys Biochem Cytol *11*, 179–205.
14. Gui, M., Ma, M., Sze-Tu, E., Wang, X., Koh, F., Zhong, E.D., Berger, B., Davis, J.H., Dutcher, S.K., Zhang, R.*, et al.* (2021). Structures of radial spokes and associated complexes important for ciliary motility. Nat Struct Mol Biol *28*, 29-37.
15. Guirao, B., Meunier, A., Mortaud, S., Aguilar, A., Corsi, J.M., Strehl, L., Hirota, Y., Desoeuvre, A., Boutin, C., Han, Y.G.*, et al.* (2010). Coupling between hydrodynamic forces and planar cell polarity orients mammalian motile cilia. Nat Cell Biol *12*, 341-350.
16. Guo, Y., Li, D., Zhang, S., Yang, Y., Liu, J.J., Wang, X., Liu, C., Milkie, D.E., Moore, R.P., Tulu, U.S.*, et al.* (2018). Visualizing Intracellular Organelle and Cytoskeletal Interactions at Nanoscale

Resolution on Millisecond Timescales. Cell *175*, 1430-1442 e1417.
17. Han, L., Rao, Q., Yang, R., Wang, Y., Chai, P., Xiong, Y., and Zhang, K. (2022). Cryo-EM structure of an active central apparatus. Nat Struct Mol Biol *29*, 472-482.
18. Herawati, E., Taniguchi, D., Kanoh, H., Tateishi, K., Ishihara, S., and Tsukita, S. (2016). Multiciliated cell basal bodies align in stereotypical patterns coordinated by the apical cytoskeleton. J Cell Biol *214*, 571-586.
19. Hirokawa, N., Noda, Y., Tanaka, Y., and Niwa, S. (2009). Kinesin superfamily motor proteins and intracellular transport. Nat Rev Mol Cell Biol *10*, 682-696.
20. Hoek, H., Klena, N., Jordan, M., Viar, G., Righetto, R., Schaffer, M., Erdmann, P., Wan, W., Geimer, S., Plitzko, J.*, et al.* (2022). In situ architecture of the ciliary base reveals the stepwise assembly of intraflagellar transport trains. Science *377*, 543–548
21. Inglis, P.N., Ou, G., Leroux, M.R., and Scholey, J.M. (2007). The sensory cilia of Caenorhabditis elegans. WormBook, 1-22.
22. Ishikawa, T. (2017). Axoneme Structure from Motile Cilia. Cold Spring Harb Perspect Biol *9*.
23. Ji, W., Tang, Z., Chen, Y., Wang, C., Tan, C., Liao, J., Tong, L., and Xiao, G. (2022). Ependymal Cilia: Physiology and Role in Hydrocephalus. Front Mol Neurosci *15*, 927479.
24. Joung, J., Konermann, S., Gootenberg, J.S., Abudayyeh, O.O., Platt, R.J., Brigham, M.D., Sanjana, N.E., and Zhang, F. (2017). Genome-scale CRISPR-Cas9 knockout and transcriptional activation screening. Nat Protoc *12*, 828-863.
25. Klena, N., and Pigino, G. (2022). Structural Biology of Cilia and Intraflagellar Transport. Annu Rev Cell Dev Biol *38*, 103-123.
26. Konjikusic, M.J., Lee, C., Yue, Y., Shrestha, B.D., Nguimtsop, A.M., Horani, A., Brody, S., Prakash, V.N., Gray, R.S., Verhey, K.J.*, et al.* (2023). Kif9 is an active kinesin motor required for ciliary beating and proximodistal patterning of motile axonemes. J Cell Sci *136*.
27. Konjikusic, M.J., Yeetong, P., Boswell, C.W., Lee, C., Roberson, E.C., Ittiwut, R., Suphapeetiporn, K., Ciruna, B., Gurnett, C.A., Wallingford, J.B.*, et al.* (2018). Mutations in Kinesin family member 6 reveal specific role in ependymal cell ciliogenesis and human neurological development. PLoS Genet *14*, e1007817.
28. Langousis, G., and Hill, K.L. (2014). Motility and more: the flagellum of Trypanosoma brucei. Nat Rev Microbiol *12*, 505-518.
29. Lechtreck, K.F. (2013). In vivo imaging of IFT in Chlamydomonas flagella. Methods Enzymol *524*, 265-284.
30. Lechtreck, K.F., Delmotte, P., Robinson, M.L., Sanderson, M.J., and Witman, G.B. (2008). Mutations in Hydin impair ciliary motility in mice. J Cell Biol *180*, 633-643.
31. Legendre, M., Zaragosi, L.E., and Mitchison, H.M. (2021). Motile cilia and airway disease. Semin Cell Dev Biol *110*, 19-33.
32. Lindemann, C.B., and Lesich, K.A. (2021). The many modes of flagellar and ciliary beating: Insights from a physical analysis. Cytoskeleton (Hoboken) *78*, 36-51.
33. Liu, H., Zheng, J., Zhu, L., Xie, L., Chen, Y., Zhang, Y., Zhang, W., Yin, Y., Peng, C., Zhou, J.*, et al.* (2021). Wdr47, Camsaps, and Katanin cooperate to generate ciliary central microtubules. Nat Commun *12*, 5796.
34. Loreng, T.D., and Smith, E.F. (2017). The Central Apparatus of Cilia and Eukaryotic Flagella. Cold Spring Harb Perspect Biol *9*.
35. Lu, W., and Gelfand, V.I. (2017). Moonlighting Motors: Kinesin, Dynein, and Cell Polarity.

Trends Cell Biol *27*, 505-514.
36. Lukinavicius, G., Reymond, L., D'Este, E., Masharina, A., Gottfert, F., Ta, H., Guther, A., Fournier, M., Rizzo, S., Waldmann, H., *et al.* (2014). Fluorogenic probes for live-cell imaging of the cytoskeleton. Nat Methods *11*, 731-733.
37. Ma, M., Stoyanova, M., Rademacher, G., Dutcher, S.K., Brown, A., and Zhang, R. (2019). Structure of the Decorated Ciliary Doublet Microtubule. Cell *179*, 909-922 e912.
38. Marshall, W.F., and Kintner, C. (2008). Cilia orientation and the fluid mechanics of development. Curr Opin Cell Biol *20*, 48-52.
39. Meleppattu, S., Zhou, H., Dai, J., Gui, M., and Brown, A. (2022). Mechanism of IFT-A polymerization into trains for ciliary transport. Cell *185*, 4986-4998 e4912.
40. Meng, X., Xu, C., Li, J., Qiu, B., Luo, J., Hong, Q., Tong, Y., Fang, C., Feng, Y., Ma, R., *et al.* (2023). High-resolution structure of mouse radial spoke and its in-situ structure in ependymal cilia revealed by cryo-EM and cryo-ET. bioRxiv.
41. Meng, Z., Meng, Q., Gao, T., Zhou, H., Xue, J., Li, H., Wu, Y., and Lv, J. (2022). Identification of bi-allelic KIF9 loss-of-function variants contributing to asthenospermia and male infertility in two Chinese families. Front Endocrinol (Lausanne) *13*, 1091107.
42. Mirzadeh, Z., Han, Y.G., Soriano-Navarro, M., Garcia-Verdugo, J.M., and Alvarez-Buylla, A. (2010). Cilia organize ependymal planar polarity. J Neurosci *30*, 2600-2610.
43. Miyata, H., Shimada, K., Morohoshi, A., Oura, S., Matsumura, T., Xu, Z., Oyama, Y., and Ikawa, M. (2020). Testis-enriched kinesin KIF9 is important for progressive motility in mouse spermatozoa. FASEB J *34*, 5389-5400.
44. Mukherjee, K., and Brocchieri, L. (2013). Ancient Origin of Chaperonin Gene Paralogs Involved in Ciliopathies. J Phylogenetics Evol Biol *1*.
45. Nachury, M.V., and Mick, D.U. (2019). Establishing and regulating the composition of cilia for signal transduction. Nat Rev Mol Cell Biol *20*, 389-405.
46. Nakayama, K., and Katoh, Y. (2018). Ciliary protein trafficking mediated by IFT and BBSome complexes with the aid of kinesin-2 and dynein-2 motors. J Biochem *163*, 155-164.
47. Nguyen, Q.P.H., Liu, Z., Albulescu, A., Ouyang, H., Zlock, L., Coyaud, E., Laurent, E., Finkbeiner, W., Moraes, T.J., Raught, B., *et al.* (2020). Comparative Super-Resolution Mapping of Basal Feet Reveals a Modular but Distinct Architecture in Primary and Motile Cilia. Dev Cell *55*, 209-223 e207.
48. Ohata, S., and Alvarez-Buylla, A. (2016). Planar Organization of Multiciliated Ependymal (E1) Cells in the Brain Ventricular Epithelium. Trends Neurosci *39*, 543-551.
49. Ohata, S., Nakatani, J., Herranz-Perez, V., Cheng, J., Belinson, H., Inubushi, T., Snider, W.D., Garcia-Verdugo, J.M., Wynshaw-Boris, A., and Alvarez-Buylla, A. (2014). Loss of Dishevelleds disrupts planar polarity in ependymal motile cilia and results in hydrocephalus. Neuron *83*, 558-571.
50. Pan, X., Fang, C., Shen, C., Li, X., Xie, L., Li, L., Huang, S., Yan, X., and Zhu, X. (2023). Basal body contains a “latchbolt” to enable directional ciliary beat across epithelia. Research Square.
51. Pigino, G. (2021). Intraflagellar transport. Curr Biol *31*, R530-R536.
52. Qiao, C., Li, D., Liu, Y., Zhang, S., Liu, K., Liu, C., Guo, Y., Jiang, T., Fang, C., Li, N., *et al.* (2022). Rationalized deep learning super-resolution microscopy for sustained live imaging of rapid subcellular processes. Nat Biotechnol.
53. Reiter, J.F., and Leroux, M.R. (2017). Genes and molecular pathways underpinning ciliopathies.

1089 Nat Rev Mol Cell Biol *18*, 533-547.
1090 54. Rogers, K.R., Weiss, S., Crevel, I., Brophy, P.J., Geeves, M., and Cross, R. (2001). KIF1D is a fast
1091 non-processive kinesin that demonstrates novel K-loop-dependent mechanochemistry. EMBO J
1092 *20*, 5101-5113.
1093 55. Ryu, H., Lee, H., Lee, J., Noh, H., Shin, M., Kumar, V., Hong, S., Kim, J., and Park, S. (2021).
1094 The molecular dynamics of subdistal appendages in multi-ciliated cells. Nat Commun *12*, 612.
1095 56. Scholey, J.M. (2013). Kinesin-2: a family of heterotrimeric and homodimeric motors with diverse
1096 intracellular transport functions. Annu Rev Cell Dev Biol *29*, 443-469.
1097 57. Siller, S.S., Sharma, H., Li, S., Yang, J., Zhang, Y., Holtzman, M.J., Winuthayanon, W.,
1098 Colognato, H., Holdener, B.C., Li, F.Q.*, et al.* (2017). Conditional knockout mice for the distal
1099 appendage protein CEP164 reveal its essential roles in airway multiciliated cell differentiation.
1100 PLoS Genet *13*, e1007128.
1101 58. Stanhope, K.T., and Ross, J.L. (2015). Microtubules, MAPs, and motor patterns. Methods Cell
1102 Biol *128*, 23-38.
1103 59. Tissir, F., Qu, Y., Montcouquiol, M., Zhou, L., Komatsu, K., Shi, D., Fujimori, T., Labeau, J.,
1104 Tyteca, D., Courtoy, P.*, et al.* (2010). Lack of cadherins Celsr2 and Celsr3 impairs ependymal
1105 ciliogenesis, leading to fatal hydrocephalus. Nat Neurosci *13*, 700-707.
1106 60. Vincensini, L., Blisnick, T., and Bastin, P. (2011). 1001 model organisms to study cilia and
1107 flagella. Biol Cell *103*, 109-130.
1108 61. Xu, Y., Cao, J., Huang, S., Feng, D., Zhang, W., Zhu, X., and Yan, X. (2015). Characterization of
1109 tetratricopeptide repeat-containing proteins critical for cilia formation and function. PLoS One *10*,
1110 e0124378.
1111 62. Yokoyama, R., O'Toole, E., Ghosh, S., and Mitchell, D.R. (2004). Regulation of flagellar dynein
1112 activity by a central pair kinesin. Proc Natl Acad Sci U S A *101*.
1113 63. Zhang, J., Wang, H., Imhof, S., Zhou, X., Liao, S., Atanasov, I., Hui, W.H., Hill, K.L., and Zhou,
1114 Z.H. (2021). Structure of the trypanosome paraflagellar rod and insights into non-planar motility
1115 of eukaryotic cells. Cell Discovery *7*.
1116 64. Zhao, C., Omori, Y., Brodowska, K., Kovach, P., and Malicki, J. (2012). Kinesin-2 family in
1117 vertebrate ciliogenesis. Proc Natl Acad Sci U S A *109*, 2388-2393.
1118 65. Zhao, H., Chen, Q., Li, F., Cui, L., Xie, L., Huang, Q., Liang, X., Zhou, J., Yan, X., and Zhu, X.
1119 (2021). Fibrogranular materials function as organizers to ensure the fidelity of multiciliary
1120 assembly. Nat Commun *12*, 1273.
1121 66. Zhao, H., Zhu, L., Zhu, Y., Cao, J., Li, S., Huang, Q., Xu, T., Huang, X., Yan, X., and Zhu, X.
1122 (2013). The Cep63 paralogue Deup1 enables massive de novo centriole biogenesis for vertebrate
1123 multiciliogenesis. Nat Cell Biol *15*, 1434-1444.
1124 67. Zheng, J., Liu, H., Zhu, L., Chen, Y., Zhao, H., Zhang, W., Li, F., Xie, L., Yan, X., and Zhu, X.
1125 (2019). Microtubule-bundling protein Spef1 enables mammalian ciliary central apparatus
1126 formation. J Mol Cell Biol *11*, 67-77.
1127

Fig.1, Fang et al.

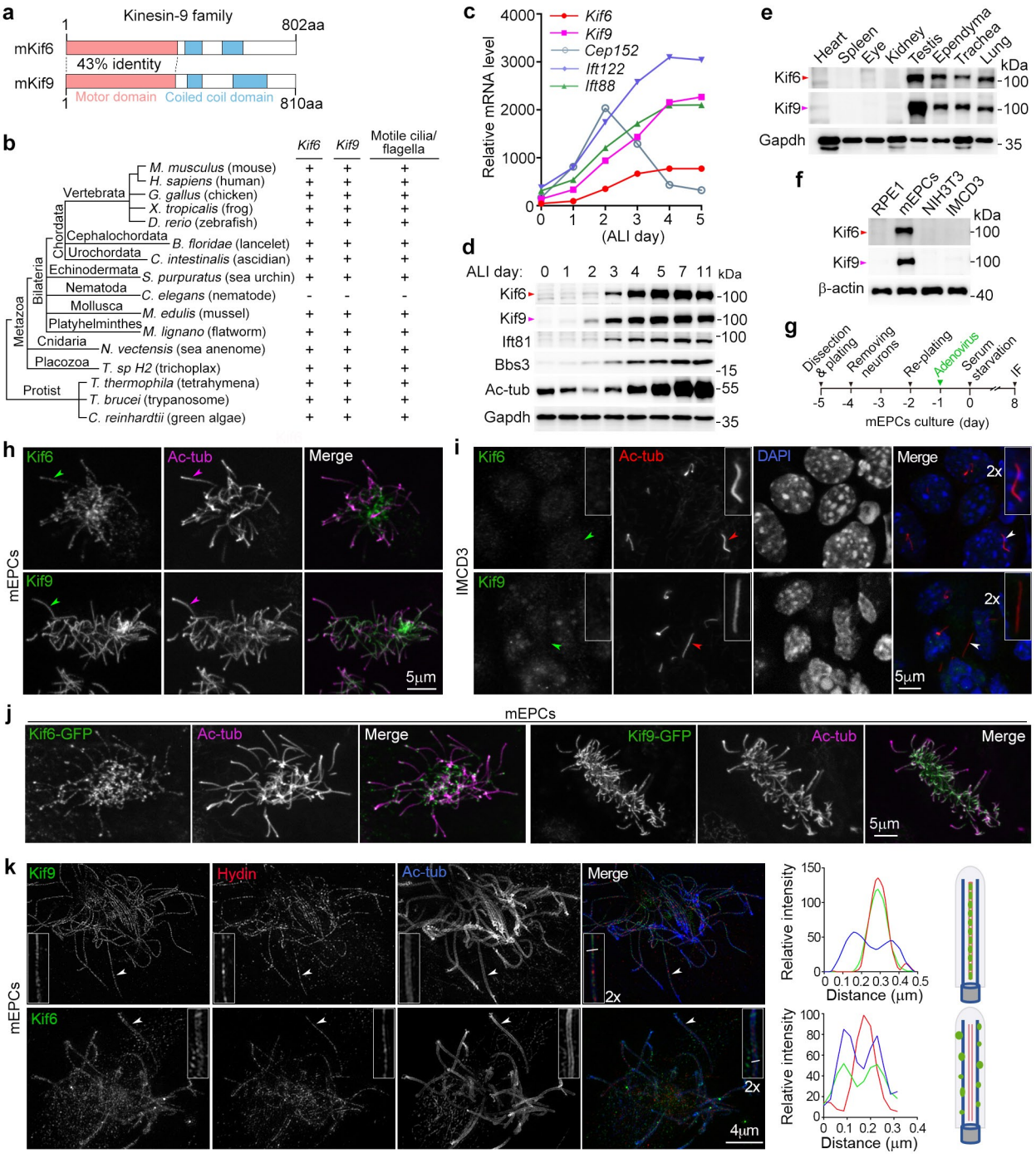

Fig. 2, Fang et al.

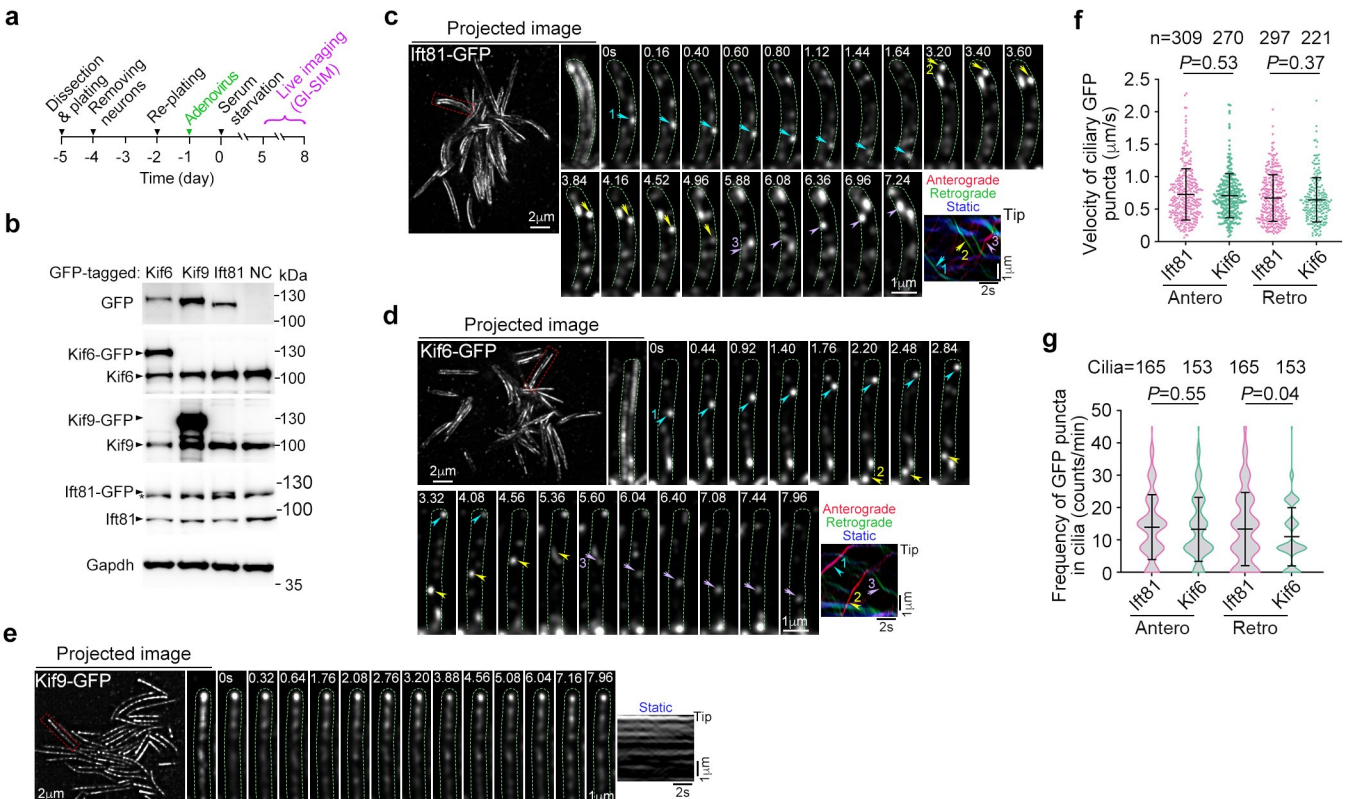

Fig. 3, Fang et al.

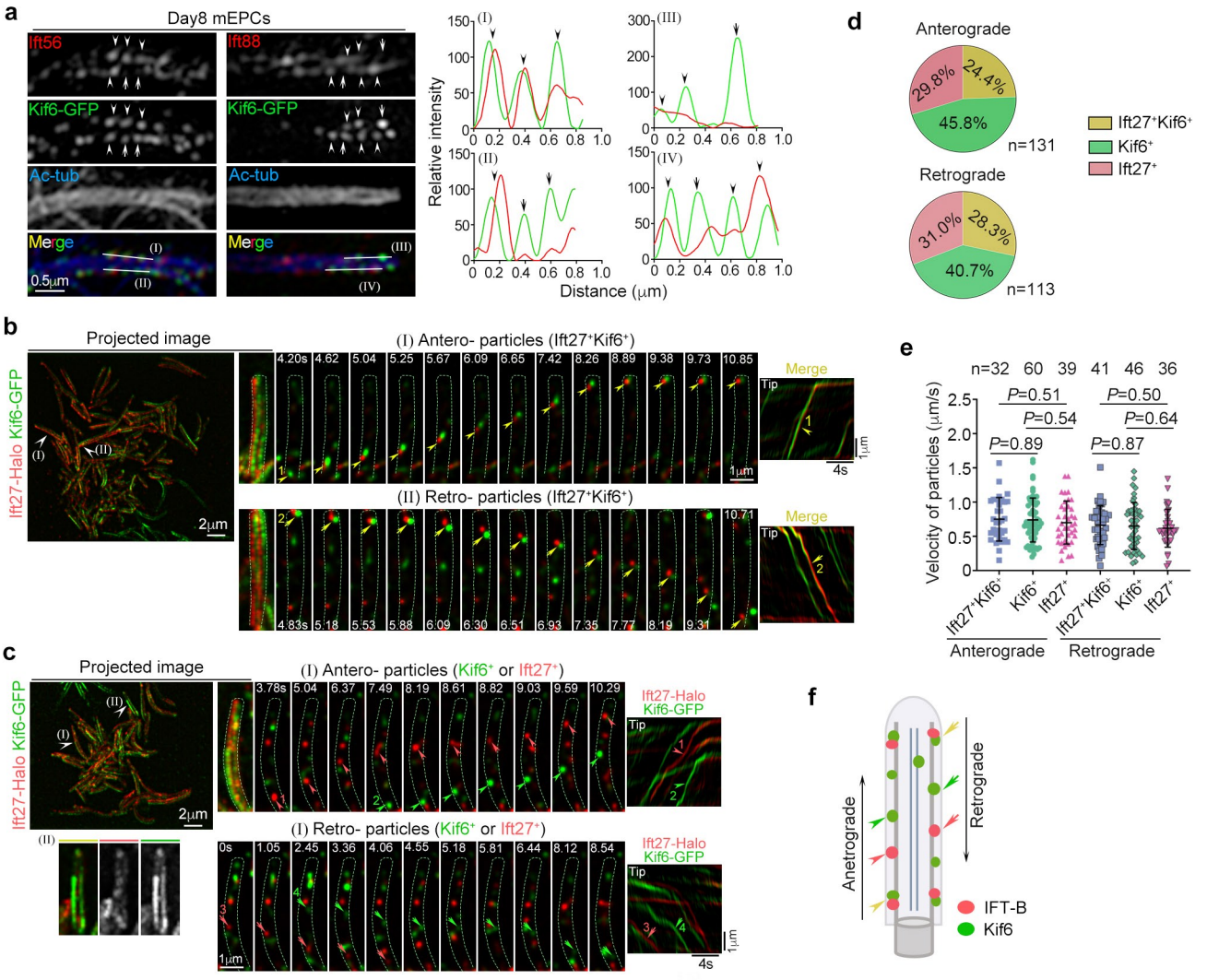

Fig. 4, Fang et al.

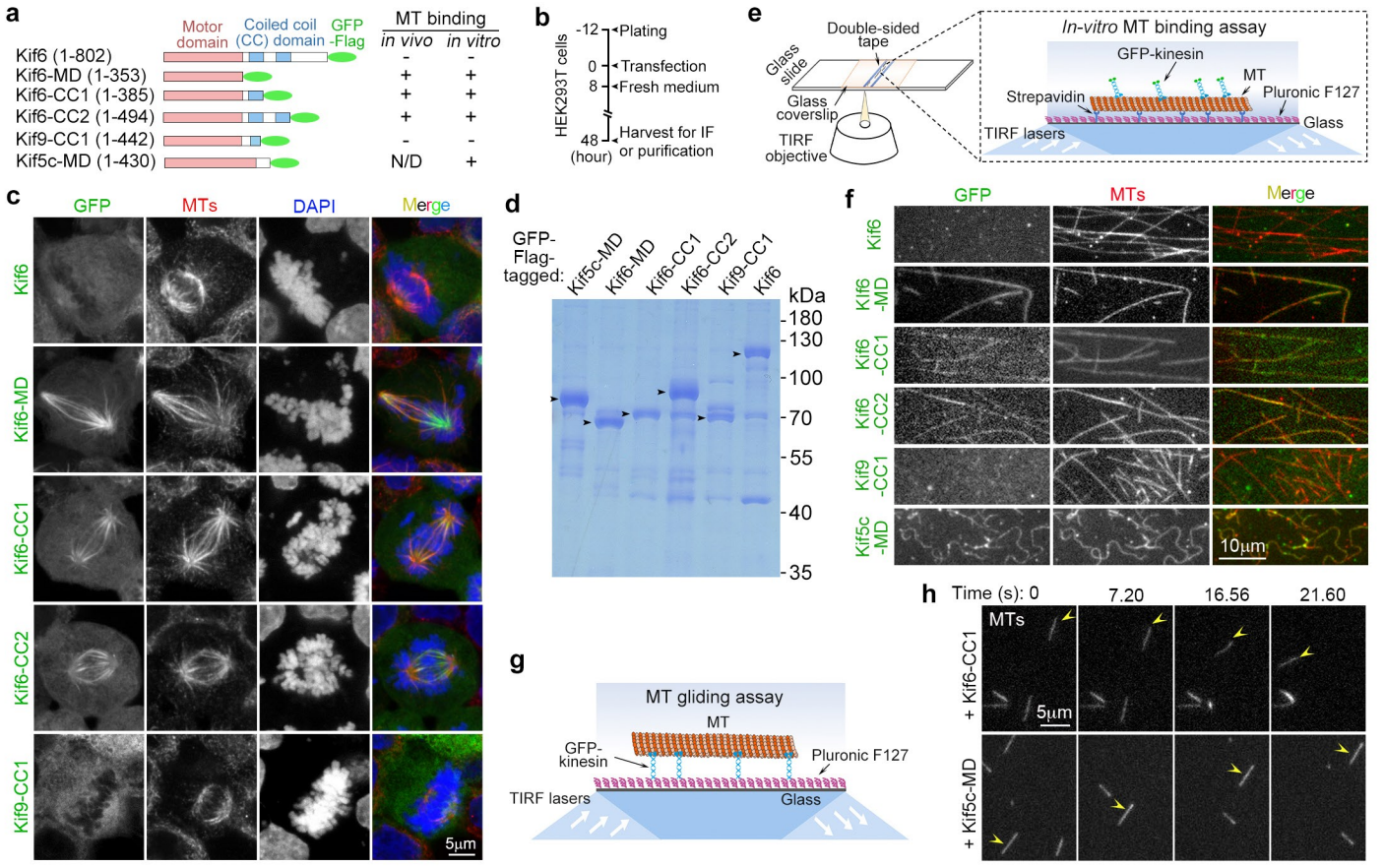

Fig. 5, Fang et al.

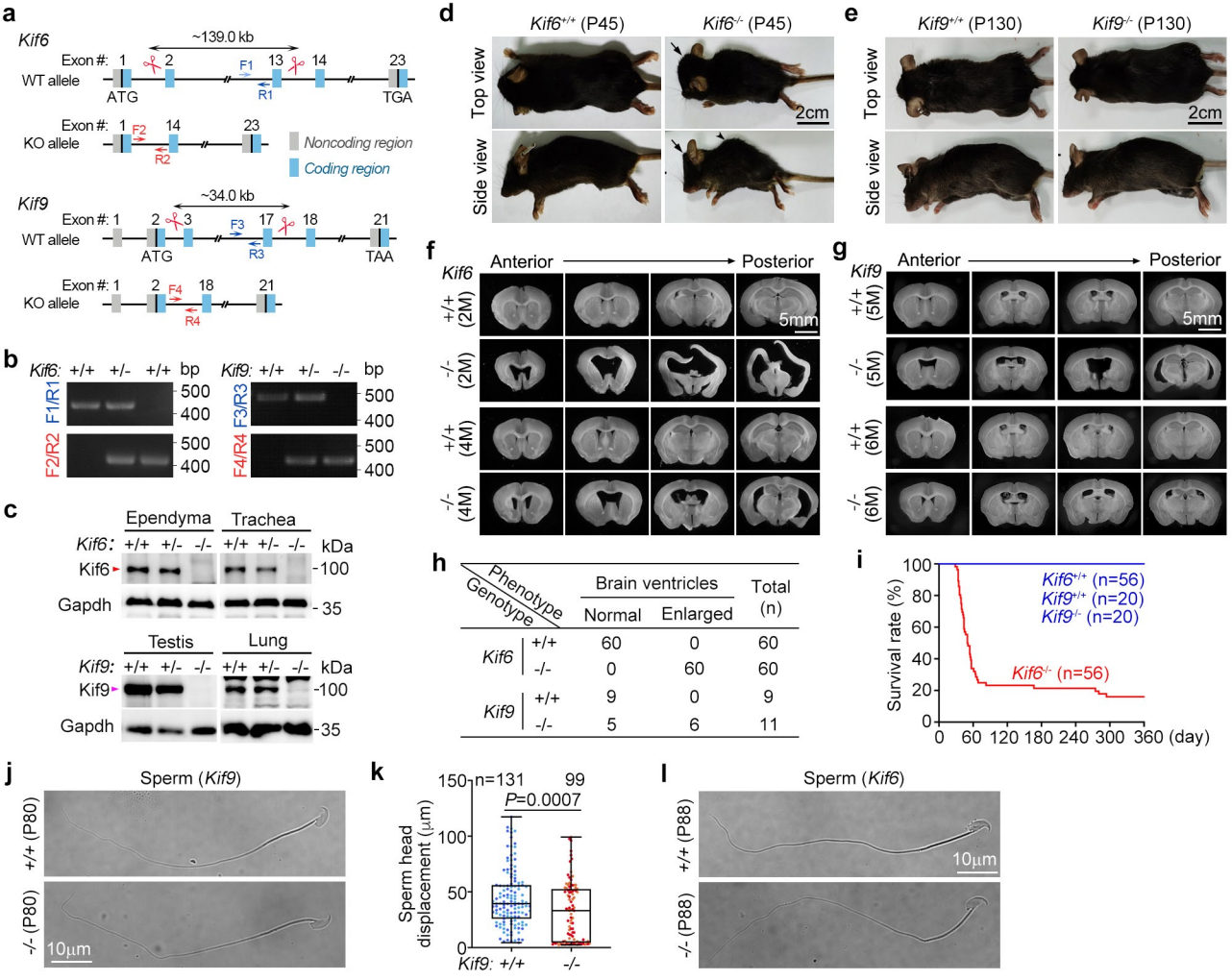

Genotype \ Phenotype		Brain ventricles: Normal	Brain ventricles: Enlarged	Total (n)
Kif6	+/+	60	0	60
	-/-	0	60	60
Kif9	+/+	9	0	9
	-/-	5	6	11

Fig. 6, Fang et al.

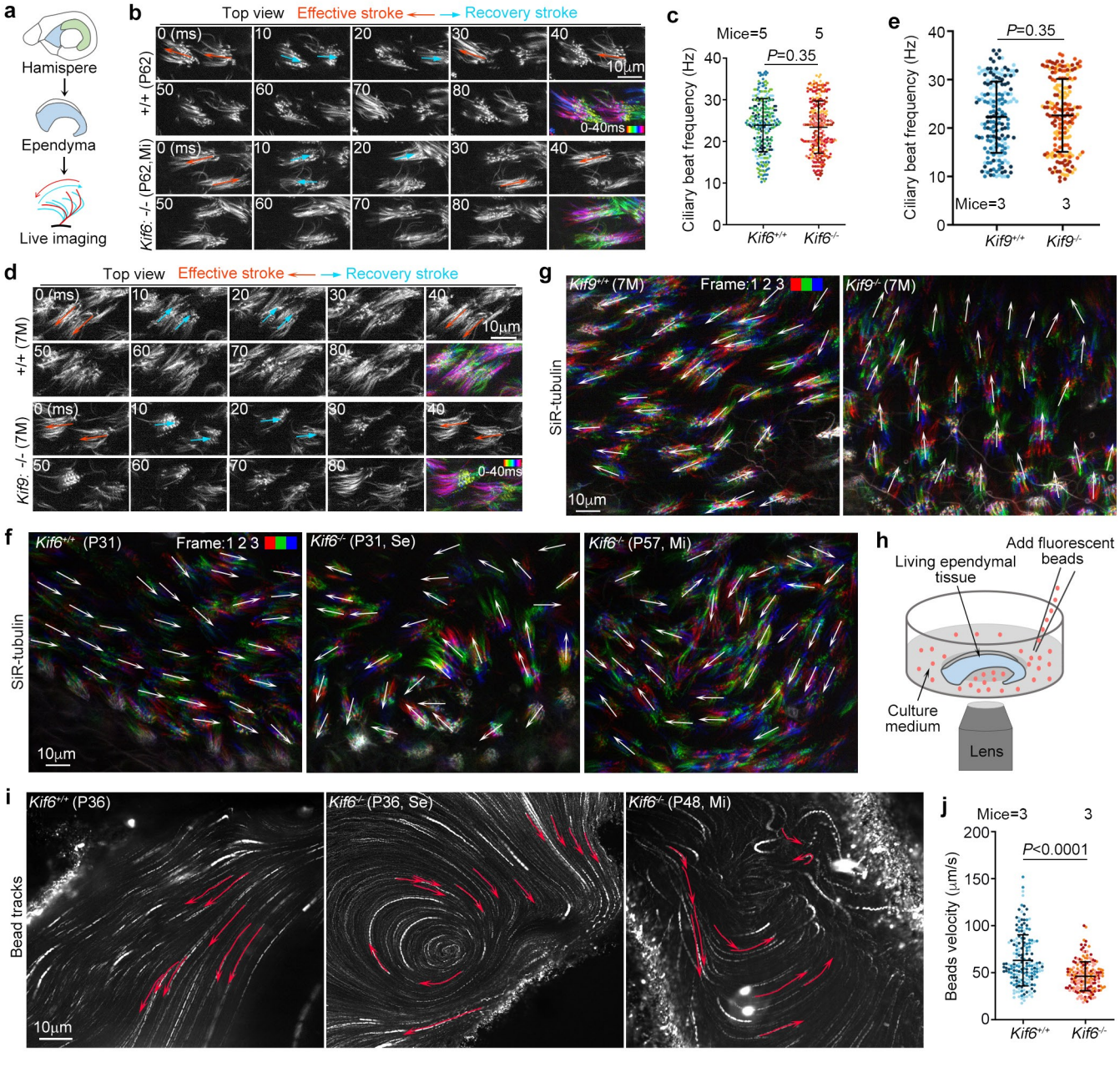

Fig. 7, Fang et al.

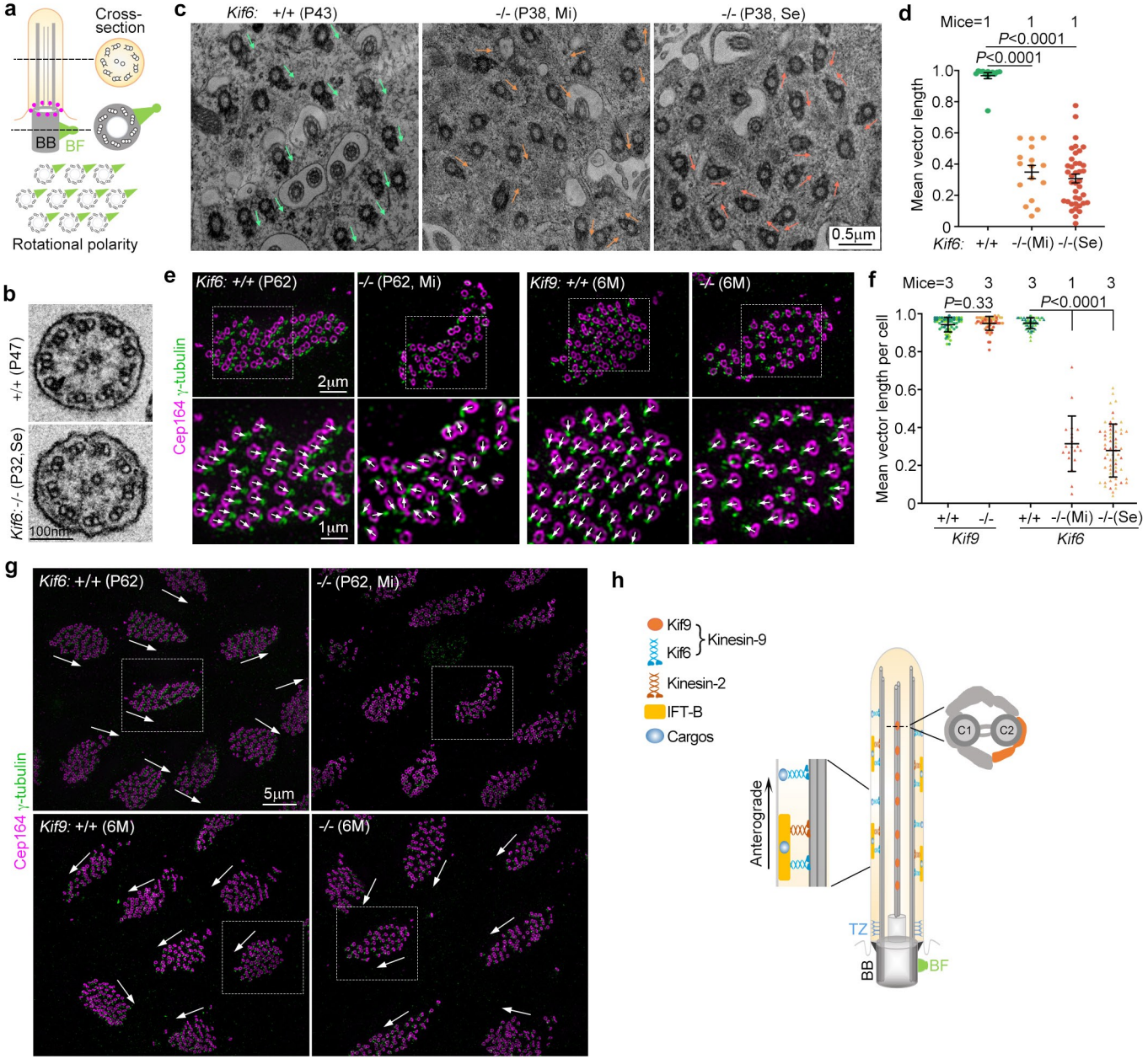

Fig.S1, Fang et al.

a

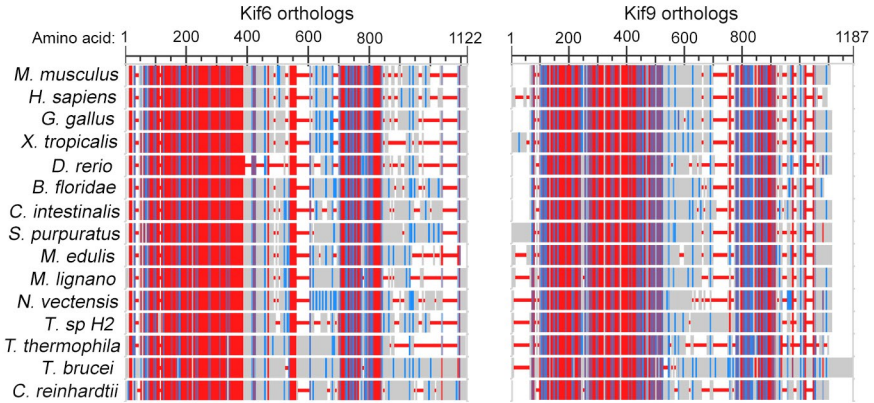

b

Motor domain

```
Kif6  1 M-VKQTIQIFARVKPTVRKQQQGIYSIDEDEKLTHSLEIVLPRDLADGFVNNKRESYKFKFQRIFDQEAKQEIIFEIIAK  79
Kif9  1 MGTRKKVQAFVRVRPT-DDFAHEMIKYGEDNK---SIDIHLKKDTRRGVVNNQQTDWSFKLDGVLHN-ASQDLVYETVAK  75

     80 PVAESTLAGYNGTIFAYGQTGSGKTFTITGGAERYSDRGIIPRTLSYIFEQLQKDSSKIYTTHISYLEIYNECGYDLLDP 159
     76 DAVSQALDGYNGTIMCYGQTGAGKTYTMTGATENYKHRGILPRALQQVFRMIEERPTHAITVRVSYLEIYNENLFDLLST 155

    160 RHEASKLEDLPKVTILEDPDQNIHLKNLSLHQATTEEEALNLLFLGDTNRMIAETPMNQASTRSHCIFTVHLS--SKEPG 237
    156 LPYVGP--SVTPMTIVENP-QGIFIKGLSVHLTSQEEDAFSLLFEGETNRIIASHTMNKNSSRSHCIFTIYMEAHSRTLS 232

    238 SATVRHAKLHLVDLAGSERVSKTGVGGLLLTEAKYINLSLHYLEQVIIALSEKHRTHIPYRNSMMTSVLRDSLGGNCMTT 317
    233 DEKYITSKINLVDLAGSERLSKTGSEGRVLKEATYINKSLSFLEQAIIALGDQNRDHVPFRQSKLTHALKDSLGGNCNMV 312

    318 MIATLSLEKRNIDESISTCRFAQRVALIKNEAILNE  353
    313 LVTNIYGEAAQLDETLSSLRFASRMKLVTTEPAINE  348
```

c

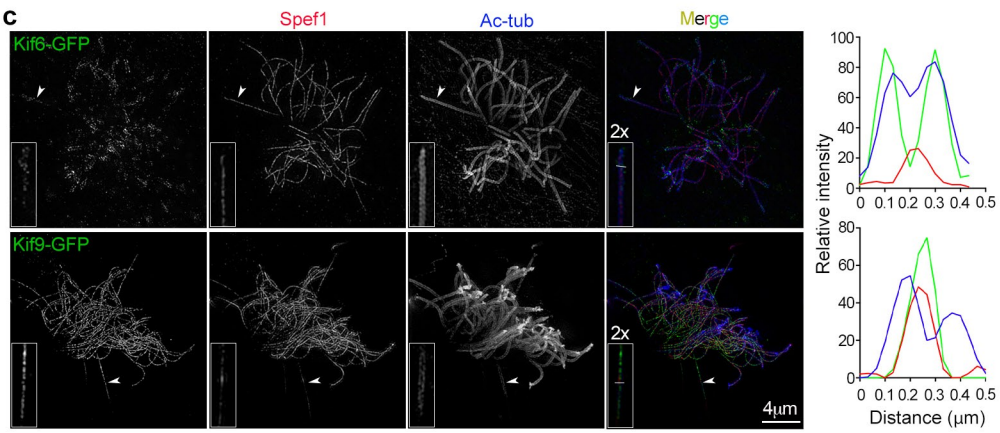

Fig. S2, Fang et al.

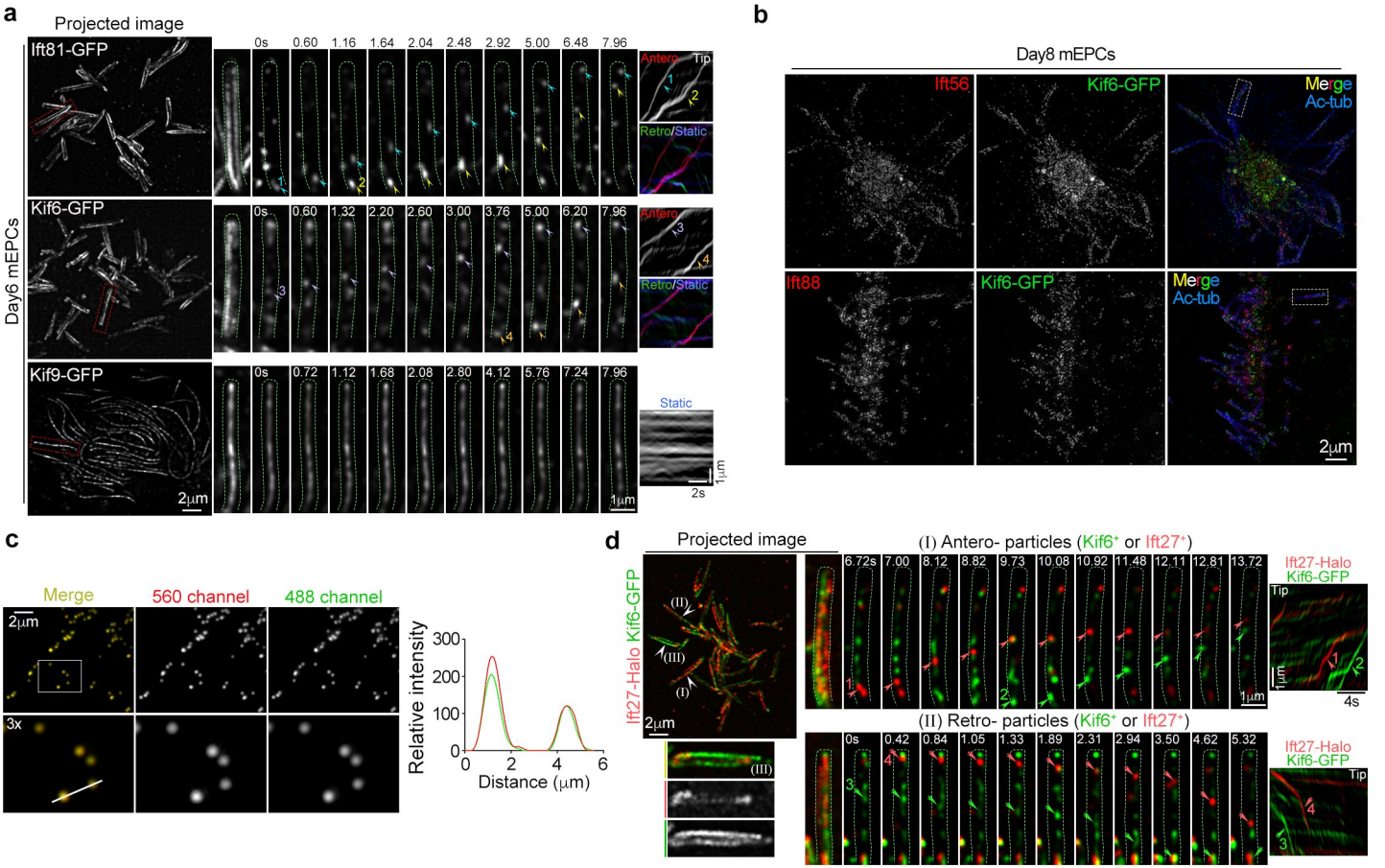

Fig. S3, Fang et al.

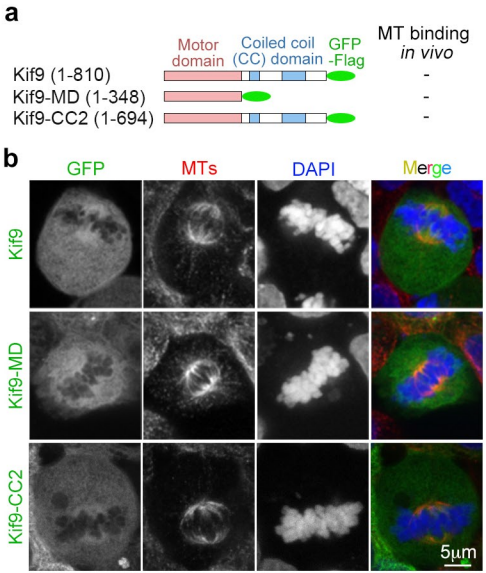

Fig. S4, Fang et al.

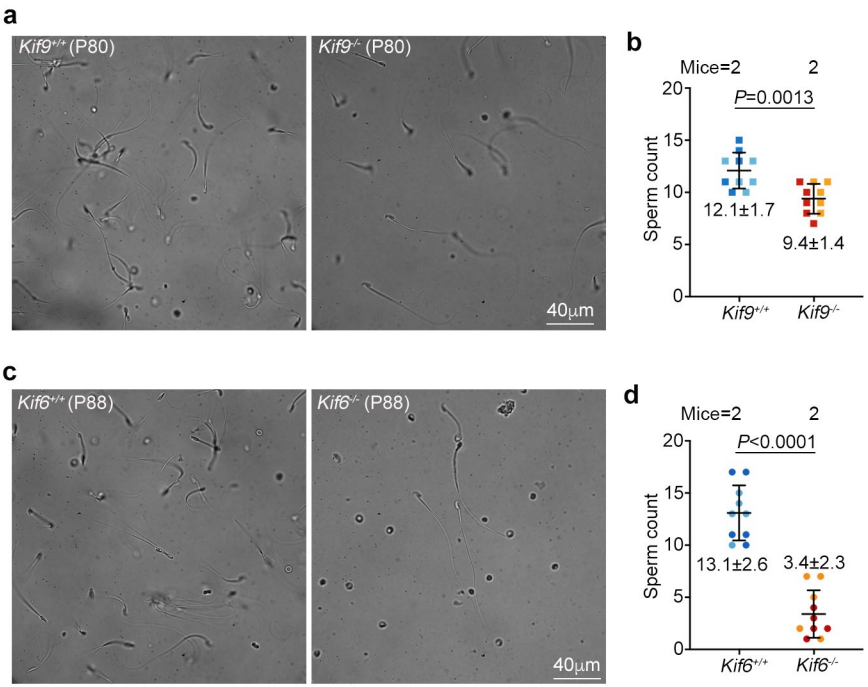
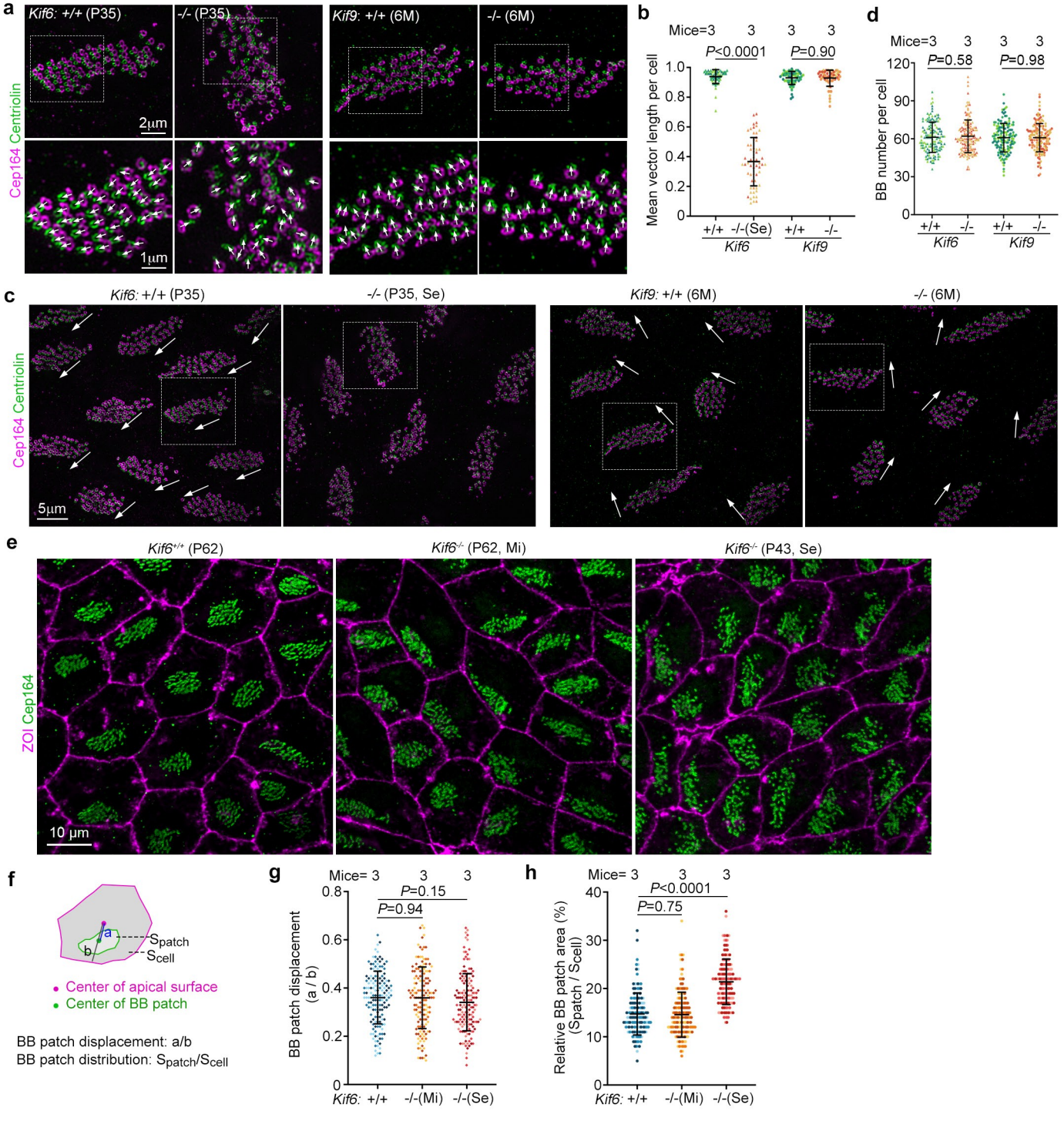
Fig. S5, Fang et al.